

AD-A188 939 AIRBORNE ELECTROMAGNETIC SOUNDING OF SEA ICE THICKNESS
AND SUB-ICE BATHYMETRY(U) COLD REGIONS RESEARCH AND
ENGINEERING LAB MANOVER NM A KOVACS ET AL. DEC 87
UNCLASSIFIED CREF-87-22 F28 8412

AD-A188 939 AIRBORNE ELECTROMAGNETIC SOUNDING OF SEA ICE THICKNESS
AND SUB-ICE BATHYMETRY(U) COLD REGIONS RESEARCH AND
ENGINEERING LAB MANOVER NM A KOVACS ET AL. DEC 87
UNCLASSIFIED CREF-87-22 F28 8412

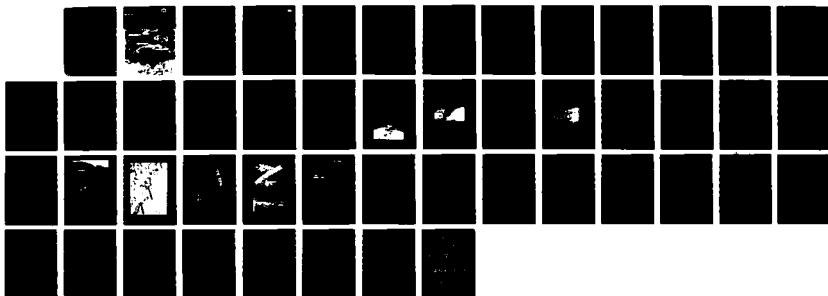
1/1

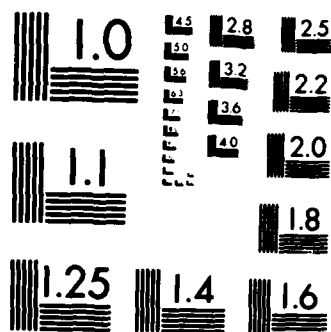
UNCLASSIFIED

ENGINEERING
CRREL-87-23

F/G 8/12

NL





MICROCOPY RESOLUTION TEST CHART
NATIONAL BUREAU OF STANDARDS 1963 A

CRREL

REPORT 87-23



4

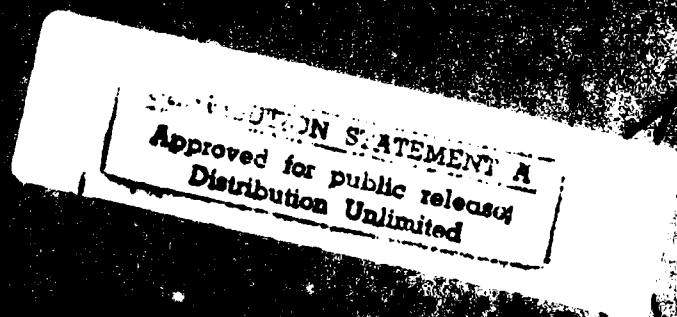
US Army Corps
of Engineers

Cold Regions Research &
Engineering Laboratory

AD-A188 939

DTIC FILE COPY

*Airborne electromagnetic sounding of
sea ice thickness and sub-ice bathymetry*



For conversion of SI metric units to U.S./British customary units of measurement consult ASTM Standard E380, Metric Practice Guide, published by the American Society for Testing and Materials, 1916 Race St., Philadelphia, Pa. 19103.

Cover: Helicopter electromagnetic sounding over sea ice. H_p represents the primary magnetic field produced by the transmit coil antenna Tx. H_s represents the secondary magnetic field resulting from eddy currents caused by the primary magnetic field flowing in a conductor, e.g. seawater. H_s is sensed by the receiver coil Rx. The in-phase and quadrature response of H_s is used to estimate the distance from the suspended antenna bird assembly to the seawater. The laser measures the distance from the bird to the snow or ice surface. From these determinations the snow and ice thickness is estimated.

CRREL Report 87-23

December 1987



Airborne electromagnetic sounding of sea ice thickness and sub-ice bathymetry

Austin Kovacs, Nicholas Valteau and J. Scott Holladay

Accession For	
NTIS CRA&I	<input checked="" type="checkbox"/>
DTIC TAB	<input type="checkbox"/>
Unannounced	<input type="checkbox"/>
Justification	
By	
Distribution /	
Availability Codes	
Dist	Avail and/or Special
A-1	



Prepared for
NAVAL OCEAN RESEARCH AND DEVELOPMENT ACTIVITY

Approved for public release; distribution is unlimited.

88 1 13 025

Unclassified

SECURITY CLASSIFICATION OF THIS PAGE

REPORT DOCUMENTATION PAGE

Form Approved
OMB No 0704-0188
Exp. Date Jun 30, 1986

1a. REPORT SECURITY CLASSIFICATION Unclassified			1b. RESTRICTIVE MARKINGS			
2a. SECURITY CLASSIFICATION AUTHORITY			3. DISTRIBUTION / AVAILABILITY OF REPORT Approved for public release; distribution is unlimited.			
2b. DECLASSIFICATION / DOWNGRADING SCHEDULE						
4. PERFORMING ORGANIZATION REPORT NUMBER(S) CRREL Report 87-23			5. MONITORING ORGANIZATION REPORT NUMBER(S)			
6a. NAME OF PERFORMING ORGANIZATION U.S. Army Cold Regions Research and Engineering Laboratory		6b. OFFICE SYMBOL (if applicable) CECRL		7a. NAME OF MONITORING ORGANIZATION Naval Ocean Research and Development Activity		
6c. ADDRESS (City, State, and ZIP Code) Hanover, New Hampshire 03755-1290			7b. ADDRESS (City, State, and ZIP Code)			
8a. NAME OF FUNDING / SPONSORING ORGANIZATION		8b. OFFICE SYMBOL (if applicable)		9. PROCUREMENT INSTRUMENT IDENTIFICATION NUMBER N6845286MP60003		
8c. ADDRESS (City, State, and ZIP Code)			10. SOURCE OF FUNDING NUMBERS			
			PROGRAM ELEMENT NO. 63704	PROJECT NO.	TASK NO.	WORK UNIT ACCESSION NO.
11. TITLE (Include Security Classification) Airborne Electromagnetic Sounding of Sea Ice Thickness and Sub-ice Bathymetry						
12. PERSONAL AUTHOR(S) Kovacs, Austin; Valleau, Nicholas; and Holladay, J. Scott						
13a. TYPE OF REPORT		13b. TIME COVERED FROM _____ TO _____		14. DATE OF REPORT (Year, Month, Day) December 1987		15. PAGE COUNT 48
16. SUPPLEMENTARY NOTATION						
17. COSATI CODES			18. SUBJECT TERMS (Continue on reverse if necessary and identify by block number) Airborne electromagnetic sounding Remote sensing Ice thickness Sea ice			
FIELD	GROUP	SUB-GROUP				
19. ABSTRACT (Continue on reverse if necessary and identify by block number) A study was made in May 1985 to determine the feasibility of using an airborne electromagnetic sounding system for profiling sea ice thickness and the sub-ice water depth and conductivity. The study was made in the area of Prudhoe Bay, Alaska. The multifrequency airborne electromagnetic sounding system consisted of control and recording electronics and an antenna. The electronics module was installed in a helicopter, and the 7-m-long tubular antenna was towed beneath the helicopter at about 35 m above the ice surface. For this electromagnetic system, both first-year and second-year sea ice could be profiled, but the resolution of ice thickness decreased as the ice became rough. This decrease was associated with the large footprint of the system, which effectively smoothed out the sea ice relief. Under-ice water depth was determined, as was seawater conductivity. The results of the feasibility study were encouraging, and further system development is therefore warranted.						
20. DISTRIBUTION / AVAILABILITY OF ABSTRACT <input checked="" type="checkbox"/> UNCLASSIFIED/UNLIMITED <input type="checkbox"/> SAME AS RPT. <input type="checkbox"/> DTIC USERS				21. ABSTRACT SECURITY CLASSIFICATION Unclassified		
22a. NAME OF RESPONSIBLE INDIVIDUAL Austin Kovacs				22b. TELEPHONE (Include Area Code) 603-646-4411		22c. OFFICE SYMBOL CECRL-EA

PREFACE

This report was prepared by Austin Kovacs, Research Civil Engineer of the Applied Research Branch, Experimental Engineering Division, U.S. Army Cold Regions Research and Engineering Laboratory; and Nicholas C. Valleau and J. Scott Holladay, Research Geophysicists, Geotech Ltd., Markham, Ontario, Canada.

Funding for this study was provided by the U.S. Department of the Navy, Naval Ocean Research and Development Activity, under contract no. N6845286MP60003, program element 63704, and in part through Geotech Ltd. internal research and development. The authors acknowledge the field assistance provided by Rexford M. Morey, Consultant, Quincy Robe of the U.S. Coast Guard Research and Development Center, and Chester F. Bassani and Victor R. Cole of Geotech Ltd. The authors also acknowledge the helpful review of this report by Dr. Alex Becker, University of California, Berkeley, and Rexford M. Morey, Consultant.

CONTENTS

	Page
Abstract	i
Preface	ii
Introduction	1
Airborne electromagnetic system	1
General theory	3
Calibration of airborne electromagnetic data	11
Field survey	12
Newly formed lead	12
Refrozen lead	13
Second-year floe	14
Grounded floeberg	20
Concluding remarks	27
Literature cited	29
Appendix A: Field survey results	31

ILLUSTRATIONS

Figure

1. Three typical AEM coil arrangements	1
2. Helicopter electromagnetic sounding over sea ice	2
3. Magnetic fields associated with AEM sensing using a horizontal coplanar coil arrangement	2
4. Transmitting and receiving coils over a layered earth	3
5. Primary electromagnetic field direction for two transmitters	4
6. Electromagnetic field response difference between a standard vertical coaxial coil pair and a whaletail horizontal coplanar coil pair	5
7. Nomogram for obtaining representative electromagnetic skin depth vs frequency and conductivity	9
8. Electromagnetic skin depth in saline water vs antenna frequency and water conductivity	10
9. Example of an Argand diagram used for determining the AEM bird elevation ..	10
10. Skim ice on a newly formed lead profiled with the AEM system	12
11. Refrozen lead profiled with the AEM system	13
12. Snow and ice thickness and under-ice water depth for a flight over a refrozen lead	13
13. AEM, laser altimeter and altitude sensor data for flight over refrozen lead	14
14. Grid layout on second-year ice floe	15
15. Aerial view of second-year ice floe	15
16. Snow and ice thickness along survey lines A, B and C, and average snow and ice thickness for the three lines	16
17. Cross section of second-year pressure ridge crossing survey lines A, B and C at about station 16	17
18. Snow and ice thickness obtained from flights 6L3 and 6L4 down the grid track on the second-year sea ice floe	18

Figure	Page
19. Snow and ice thickness obtained from flights 8L2, 8L3 and 8L4 down the grid track on the second-year sea ice floe.	18
20. Location of grounded ice formations on Cat Shoals, and of Loon Shoal, Sand-piper and North Star islands, and AEM sounding track 6L7.	20
21. View of south side of grounded rubble formation C and its highest ridge.	21
22. Extremely high rubble formation found grounded in 1984 on a shoal north of Oliktok Pt.	21
23. Aerial view of grounded rubble formations B, C and D in August 1984.	22
24. Aerial view of grounded rubble formations B and C in March 1985.	23
25. Floeberg C, showing the location of the highest ridge and the lines along which the topography was determined via stereo analysis.	24
26. Aerial view of floebergs B, C and D.	24
27. North of floeberg C and its highest ridge.	25
28. AEM profile results from the flight over floeberg C.	25
29. Snow and ice elevation profiles as determined by stereo analysis techniques.	26
30. AEM profile results obtained from flight 6L7.	27

TABLE

Table

1. Average snow and ice thickness and seawater conductivity for each flight over the second-year ice floe.	19
---	----

Airborne Electromagnetic Sounding of Sea Ice Thickness and Sub-ice Bathymetry

AUSTIN KOVACS, NICHOLAS C. VALLEAU AND J. SCOTT HOLLADAY

INTRODUCTION

In May 1985, a multifrequency, multicoil-geometry airborne electromagnetic (AEM) system was used for the first time for estimating sea ice thickness, water conductivity, and water depths from about 1 to 20 m under an ice cover. The AEM system was basically a standard geophysical exploration device used for recognizing and analyzing changes in the earth's conductivity. The technology makes use of the fact that penetration of electromagnetic waves into conductive materials is frequency-dependent, as are the return amplitude and phase spectra measured at a receiving antenna (e.g. Grant and West 1965, Keller and Frischknecht 1966, Kaufman and Keller 1983). It is an airborne technology that has been used by industry for several decades for detecting and mapping conductive mineral deposits (e.g. Pemberton 1962, Ward 1970, Fraser 1981).

The concept of using this technology for measuring coastal bathymetry was reviewed by Morrison and Becker (1982) and for detecting sea ice thickness by Becker et al. (1983). The feasibility of using an AEM system for measuring sea ice thickness perhaps originated in 1968 (Anon.) but was not pursued beyond an analytical study. However, this analysis verified that both thin and thick sea ice could be measured, though the paper cautioned that pressure ridges would pose a problem because of their three-dimensional nature. The study also mentioned the need for a system having high resolution and a very rapid response time, since many pack ice features (for example, leads and ridges) will be flown over in seconds or fractions of a second.

This paper presents results of our 1985 study which determined the feasibility of using an AEM system for profiling sea ice thickness, seawater conductivity and under-ice water depth. The field program included AEM measurements over a second-year sea ice floe of known thickness as well as first-year sea ice of several thicknesses. Also sounded were four very long and thick second-year sea ice floebergs grounded on a shoal.

Airborne electromagnetic system

The AEM system used in this study had four pairs of coils (transmitter *Tx* and receiver *Rx*). The coils behave as magnetic dipoles and, along with system electronics, allow simultaneous operation at four distinct frequencies in two coil configurations, horizontal coplanar and vertical coaxial (Fig. 1). The nominal operating frequencies were 530 and 16,290 Hz (horizontal coplanar) and 930 and 4,160 Hz (vertical coplanar). A fifth frequen-

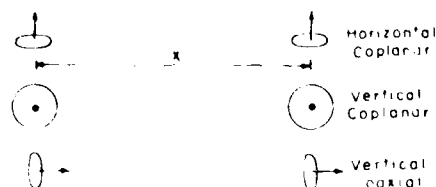


Figure 1. Three typical AEM coil arrangements. Arrows indicate the magnetic dipole orientation.

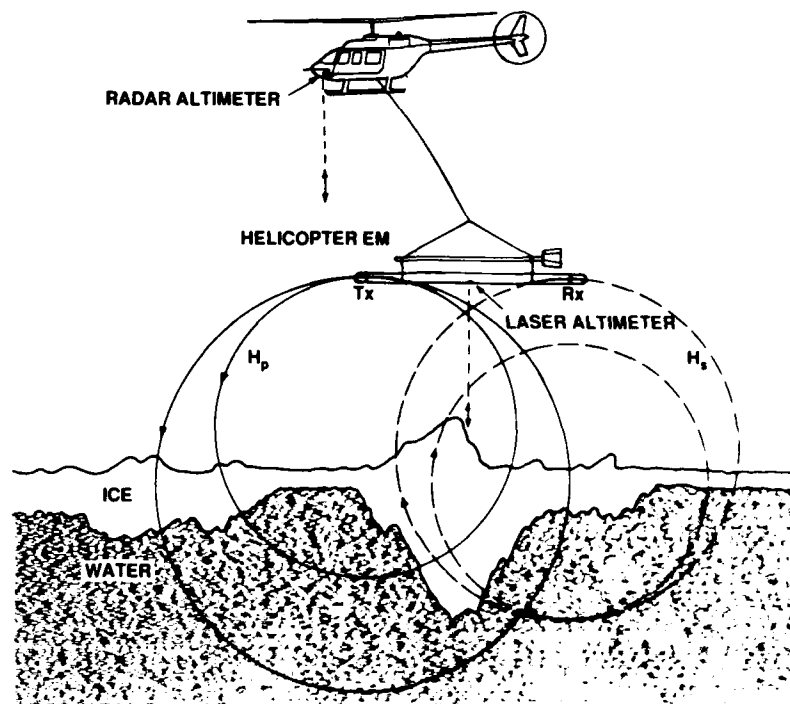


Figure 2. Helicopter electromagnetic sounding over sea ice.

cy of 32,020 Hz was also evaluated by replacing the 16,290-Hz coils in the field. The transmitter and receiver coils were about 6.5 m apart inside a Kevlar tube (called a "bird") about 7.5 m long and 0.5 m in diameter. The bird weighed about 200 kg and was typically flown about 35 m above the ice surface (Fig. 2).

In principle, the transmitter coil produces a primary magnetic field H_p , which causes eddy currents to flow in nearby conductors (e.g. seawater). The resulting secondary H_s and primary magnetic fields are sensed by the receiver coils (Fig. 3). The distance to and conductivity of a conductive medium affect the mutual coupling ratio H_s/H_p . Through the use of bucking coils in the bird and system electronics, the primary field at the receiver is cancelled out, and highly precise measurements of the in-phase (*IP*) and quadrature (*Q*) components of the secondary magnetic field are made and recorded. The measurements are expressed in parts per million (ppm) of the primary field that would have been sensed by the receiver if bucking were not performed. These data, along with frequency, T_x and R_x coil spacing and orientation, and bird pitch and roll sensor data, are then used to calculate an apparent conductivity σ and bird height above the conductive surface.

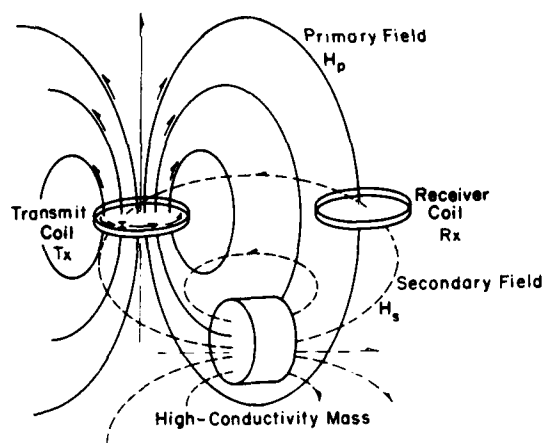


Figure 3. Magnetic fields associated with AEM sensing using a horizontal coplanar (whaletail) coil arrangement.

Since sea ice is relatively resistive and therefore transparent at the AEM system's lower frequencies, the system senses the conductive seawater and thus determines the distance from the bird to the sea surface. A laser profilometer system was built into the bird and used to measure the distance from the bird to the ice surface. Subtracting this distance from the distance to the seawater surface determined by the AEM system gives the apparent ice thickness, or the snow and ice thickness where a snow cover exists.

A radar altimeter was installed on the helicopter, and a radar elevation display was mounted in front of the pilot to help him maintain an altitude of about 65 m above the ice surface. Since the bird is suspended 30 m below the helicopter, the bird was flown about 35 m above the ice relief.

A flight-path video recorder system was also installed on the helicopter. The camera was mounted to view the bird in flight and the terrain being overflown. This information was available for post-flight review and for real-time viewing in the helicopter.

General theory

There are a number of ways to represent the responses of a stratified earth, consisting of n layers, to an oscillating magnetic dipole elevated above the earth's surface. For the example in Figure 4, T_x is the magnetic source dipole at height h_1 , R_x is the magnetic sensor at height h_2 , x is the horizontal distance between the electrical center of the T_x and R_x coils, and $\sigma_1 \dots \sigma_n$ are layer conductivities (S/m) of thickness $t_1 \dots t_n$. Maxwell's equations describe the behavior of the electromagnetic field as follows (for a general case):

$$\nabla \cdot \epsilon \vec{E} = \rho_f \quad (1)$$

$$\nabla \cdot \mu \vec{H} = 0 \quad (2)$$

$$\nabla \times \vec{E} + j\omega \mu \vec{H} = 0 \quad (3)$$

$$\nabla \times \vec{H} - j\omega \epsilon \vec{E} = \vec{J} \quad (4)$$

where $\nabla \cdot$ = vector divergence

$\nabla \times$ = curl of the vector field

ϵ = relative permittivity (normally $\epsilon = \epsilon_0$ = free-space permittivity = 8.854×10^{-12} F/m)

\vec{E} = electric field intensity (V/m)

ρ_f = free charge density (C/m³)

\vec{H} = magnetic field intensity (A/m)

μ = relative magnetic permeability (normally $\mu = \mu_0$ = free-space magnetic permeability = $4\pi \times 10^{-7}$ H/m)

ω = angular frequency = $2\pi f$

f = frequency (Hz)

\vec{J} = current density (A/m²)

$j = \sqrt{-1}$.

A quasi-static long-wave length approximation is employed in which displacement currents are considered to be negligible in comparison with conduction currents in the model, and the free-space wavelength is very long compared to scale lengths.

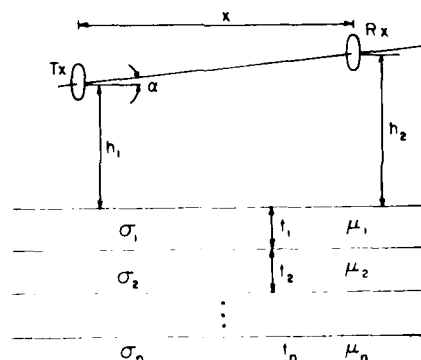
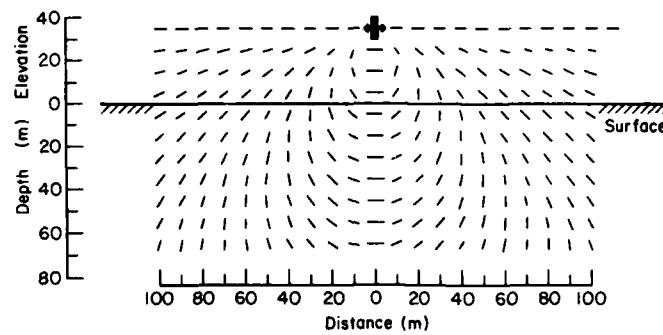
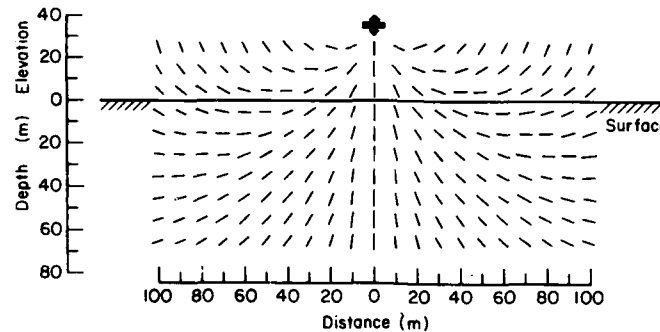


Figure 4. Transmitting and receiving coils over a layered earth.



a. Coaxial transmitter.



b. Coplanar transmitter.

Figure 5. Primary electromagnetic field direction for two transmitters. Arrows indicate the magnitude dipole orientations. (After Fraser 1979.)

This is valid as long as $\omega\epsilon \ll \sigma_a$, where σ_a is the average conductivity, and the ϵ of the model is on the order of 7×10^{-10} F/m. Since typical AEM system bandwidths are less than 50 kHz and scale lengths are normally much less than the wavelength of 50-kHz radiation, the quasi-static approximation is valid for most AEM sounding problems.

Helicopter AEM systems normally employ one or more of the three coil configurations depicted in Figure 1. There are other coil arrangements. A loop senses fields crossing its plane as described by Faraday's Law (eq 3) and is only sensitive to field components perpendicular to its plane. Because of this, the amplitude response of a stratified earth to a vertical electromagnetic dipole (whaletail configuration) elevated above the surface is significantly different from that of a dipole in the horizontal plane (fishtail or coaxial configuration). The primary magnetic field under the vertical coil is essentially horizontal (Fig. 5). This orientation provides excellent coupling to steeply dipping bodies. The primary magnetic field under a horizontal coil is essentially vertical and therefore couples well with a horizontal conductor (Fraser 1979). Figure 6 illustrates the coupling responses of vertical (standard) coaxial and horizontal coplanar (whaletail) coil pairs as they move up to and beyond vertical and inclined conductors. Related response variations obtained with the use of a multicoil AEM system allow for detection and an assessment of the depth and slope of a conductive body or interface. Magnetic dipoles are convenient mathematical approximations for describing the response of loop-type transmitters, and coil receivers are commonly used as sensors for the magnetic field. Maxwell's equations (eq 1-4) are now combined to form the electromagnetic wave equations in \vec{E} and \vec{H} :

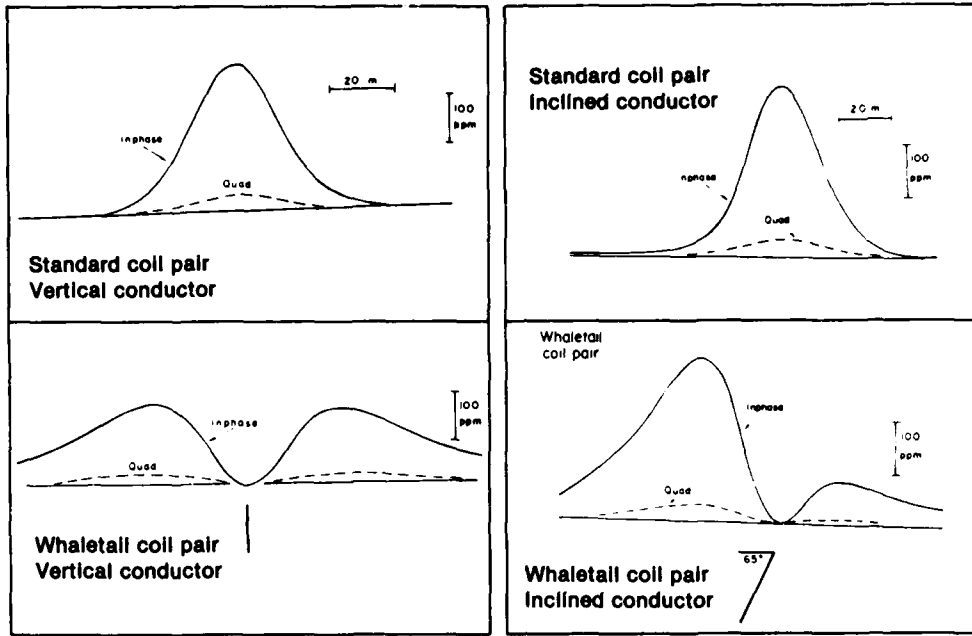


Figure 6. Electromagnetic field response difference between a standard vertical coaxial coil pair and a whaletail horizontal coplanar coil pair moved across a vertical and an inclined dike conductor. The peak of the EM response for the standard coil pair and the trough for the whaletail coil pair are shown to be centered over the dike. (After Fraser 1979.)

$$\nabla^2 \bar{E} = j\sigma\mu\omega \bar{E} - \epsilon\mu\omega^2 \bar{E} \quad (5a)$$

$$\nabla^2 \bar{H} = j\sigma\mu\omega \bar{H} - \epsilon\mu\omega^2 \bar{H}. \quad (5b)$$

Under the quasi-static approximation these expressions become diffusion equations:

$$\nabla^2 \bar{E} = j\sigma\mu\omega \bar{E} \quad (6a)$$

$$\nabla^2 \bar{H} = j\sigma\mu\omega \bar{H} \quad (6b)$$

which for a nonconducting medium reduce to

$$\nabla^2 \bar{E} = 0 \quad (7a)$$

$$\nabla^2 \bar{H} = 0. \quad (7b)$$

Equations 6a and b are Helmholtz expressions with wave number $k^2 = -j\mu\omega\sigma$.

Solutions to these equations can be derived in terms of potentials suited to the particular problem and then differentiated to give the behavior of the fields themselves. Examples of this process can be found in Wait (1951). They are often expressed as coupling ratios in which the mutual coupling Z_T of two coils, the magnetic Tx dipole and the receiver coil, is normalized by the "free-space" coupling ratio, for the same coil configuration, as follows (Verma 1982):

$$Z_T = \frac{V_{Rx}}{I_{Tx}} = \frac{-j\mu\omega a H_T}{I_{Tx}} \quad (8)$$

where V_{Rx} = voltage at receiver coil

I_{Tx} = current in Tx coil

a = effective area of coil

H_T = total magnetic field sensed by Rx coil.

For the coplanar and coaxial loops illustrated in Figure 1, the free-space coupling ratio values are, respectively,

$$Z_0(\text{cop}) = +j\omega\mu_0 a_1 a_2 / 4\pi x^3 \quad (9a)$$

$$\begin{aligned} Z_0(\text{coax}) &= -j\omega\mu_0 a_1 a_2 / 2\pi x^3 \\ &= -2Z_0(\text{cop}) \end{aligned} \quad (9b)$$

where a_1 and a_2 represent the effective area of coils one and two, respectively, and x is the distance between coils.

The secondary coupling ratio Z_s is similarly defined as

$$Z_s = -j\omega\mu a H_s / I_{Tx} \quad (10)$$

where H_s is the secondary magnetic field at the receiver coil, which is just the total magnetic field minus the primary free-space field:

$$\frac{Z_s}{Z_0} = \frac{Z_T}{Z_0} - 1. \quad (11)$$

The secondary coupling ratio just expresses the secondary magnetic field as a function of the primary field. It is this ratio, expressed in ppm, that was determined from the AEM profile data.

Verma (1982) reviewed one approach for computing these coupling ratios and provided a convenient summary of the so-called Hankel integrals T_0 , T_1 and T_2 used in the calculation. These integrals are defined as follows:

$$T_0(x, \underline{t}, \underline{\sigma}, f) = \int_0^\infty R_0(\underline{t}, \underline{\sigma}, \lambda) \lambda^2 e^{-\lambda(h_1 + h_2)} \cdot J_0(\lambda x) d\lambda \quad (12)$$

$$T_1(x, \underline{t}, \underline{\sigma}, f) = \int_0^\infty R_0(\underline{t}, \underline{\sigma}, \lambda) \lambda^2 e^{-\lambda(h_1 + h_2)} \cdot J_1(\lambda x) d\lambda \quad (13)$$

$$T_2(x, \underline{t}, \underline{\sigma}, f) = \int_0^\infty R_0(\underline{t}, \underline{\sigma}, \lambda) \lambda e^{-\lambda(h_1 + h_2)} \cdot J_1(\lambda x) d\lambda \quad (14)$$

where \underline{t} = vector of layer thickness

$\underline{\sigma}$ = vector of layer conductivity

λ = spatial wave number

J_0, J_1 = zeroth- and first-order Bessel function, respectively

h_1, h_2 = height of Tx and Rx, respectively (Fig. 4)

R_0 = reflection coefficient, defined recursively by Koefoed (1972) as

$$R_{i-1,n}(\underline{t}, \underline{\sigma}, \lambda) = \frac{V_{i-1,i} + R_{i,n} e^{-2q_i V_i}}{1 + V_{i-1,i} R_{i,n} e^{-2q_i V_i}} \quad (15)$$

where $R_{n,n} = 0$

$$\begin{aligned} V_i &= \sqrt{\lambda^2 + k_i^2} \\ k_i &= \sqrt{-j\omega\mu\sigma_i} \\ V_{i,k} &= (V_i - V_k)/(V_i + V_k). \end{aligned}$$

The horizontal coplanar, vertical coplanar and vertical coaxial loop secondary coupling ratios are now, respectively

$$\frac{Z}{Z_0} = x^3 T_0 \quad (16)$$

$$\frac{Z}{Z_0} = x^3 T_1 \quad (17)$$

$$\frac{Z}{Z_0} = x^3 (T_1 - xT_0)/2. \quad (18)$$

The technique reviewed by Verma (1982) and first used by Ghosh (1971) is commonly called the "linear digital filter" method. It permits the computation of rapid, stable estimates of the electromagnetic response of a layered earth model. The technique works very well and serves as an excellent basis for a general forward and inverse modeling technique. However, for our AEM interpretation requirements, his approach represents "overkill." A much faster method for performing the integrals (eq 12-14) was used, based on Gauss-Laguerre integration of the Hankel transforms. Gauss-Laguerre is a standard technique of numerical analysis. The integrals are performed five to ten times faster than for the shortest acceptable digital filter evaluated. Since the inversion process spends most of its time on the evaluation of the Hankel transform integrals, the inversion is also speeded up by a factor of five to ten.

The inversion method we used to analyze the AEM data is based on a standard numerical technique of least-squares nonlinear regression with singular value truncation and damping, optimized for ice and water depth interpretation. All four frequencies (eight channels) of AEM data are used together in the inversion process. It is a generalized and enhanced version of the Gauss-Newton and Marquardt methods (Marquardt 1963). Consider the computed response \underline{C} of a layered earth model, a known nonlinear function of the model parameter \underline{g} , \underline{t} and \underline{p} :

$$\underline{C} = F(\underline{g}, \underline{t}, \underline{p}) \quad (19)$$

where \underline{p} represents the system parameters such as coil separation, frequencies, altitude, pitch, roll, etc. However, F can be approximately linearized by a Taylor series expansion in the model parameters \underline{g} and \underline{t} . Thus, if \underline{X} represents the desired model parameters (including perhaps both \underline{g} and \underline{t}), F can be expressed as the infinite series

$$F(\underline{X} - \underline{X}_0) = F(\underline{X}_0) + \frac{\partial F(\underline{X}_0)}{\partial \underline{X}} \cdot (\underline{X} - \underline{X}_0) + \frac{\partial^2 F(\underline{X}_0)}{\partial \underline{X}^2} \cdot (\underline{X} - \underline{X}_0)^2 + \dots \quad (20)$$

where \underline{X}_0 represents a set of parameters for the "starting model" in the inversion. With the starting model \underline{X}_0 "close" to the true model \underline{X} , the series can be approximated by truncation to the first-order term

$$F(\underline{X} - \underline{X}_0) \cong F(\underline{X}_0) + \frac{\partial F(\underline{X}_0)}{\partial \underline{X}} \cdot (\underline{X} - \underline{X}_0). \quad (21)$$

This "linearization" process is now set up in terms of the residual response $\underline{\Delta C} = \underline{0} - \underline{C}$ and a parameter correction vector $\underline{\Delta X} = \underline{X} - \underline{X}_0$, where \underline{X}_0 is now the base model for this step of the inversion process, $\underline{0}$ is a set of observations and $\underline{C} = F(\underline{X}_0)$. Then, from eq 21 we obtain

$$\underline{\Delta C} = \frac{\partial F(\underline{X}_0)}{\partial \underline{X}} \cdot \underline{\Delta p} \quad (22)$$

in which $\partial F/\partial \underline{X}$ is the Jacobian matrix $J_{ij} = \partial f_i/\partial X_j$, where $f_i(X) = C_i$. This matrix is normally non-negative definite and cannot always be inverted, even with infinite-precision arithmetic, because of the zero eigenvalues that it may possess. To get around this problem, approximate inverses are used (Jupp and Vozoff 1957, Holladay 1980). Briefly the matrix is decomposed into two eigenvector matrices and a set of singular values. This process is called the singular value decomposition by Lanczos (1961) and is expressed

$$\mathbf{J} = \mathbf{U} \mathbf{\Lambda} \mathbf{V}' \quad (23)$$

where \mathbf{J} = Jacobian matrix

\mathbf{U} = data eigenvector

\mathbf{V} = parameter vector

$\mathbf{\Lambda}$ = diagonal matrix of singular values for \mathbf{J} .

In this process, rows and columns of \mathbf{U} and \mathbf{V} corresponding to zero and near-zero singular values are discarded, and damping is applied to the remaining singular values as required. The damped matrix is then inverted to give a solution

$$\underline{\Delta X} = \mathbf{V} \mathbf{\Lambda}^{-1} \mathbf{U}' \underline{\Delta C} \quad (24)$$

which is used to correct the parameter vector \underline{X} . Then a new forward model $\underline{F}(\underline{X})$ is computed, a new residual $\underline{\Delta C}$ is formed, and the process is repeated until

$$|\underline{\Delta C}| = \sqrt{\underline{\Delta C}' \cdot \underline{\Delta C}} \quad (25)$$

falls within acceptable limits.

The starting model is fairly important to the efficiency of the process. Indeed, if the starting model is too "far" from the true solution, the process may not converge. To avoid this problem, a table was used to prepare a good starting model.

The above analysis will always allow determination of the distance from the AEM bird to the seawater surface, provided the bird is flown within a prescribed elevation window. This elevation window is dictated by the AEM system response, sensitivity and dynamic range, and is generally 20–50 m above the surface. Flying the bird below about 20 m may cause the electromagnetic field strength from seawater to saturate the receiver. This can be overcome by reducing the receiver sensitivity but currently not in real time. Flying the bird higher than about 50 m can cause the electromagnetic field from the seawater to be too weak to measure accurately. As an examination of the EM response equations will show, the electromagnetic bathymetry problem will not always allow for accurate inversion. There is the problem of screening by the conductive seawater and, to a much lesser extent, by conductive sea ice. As the electromagnetic wave penetrates the ice and water, it is attenuated and phase-rotated. Reflections from the water surface and from the seabed are likewise attenuated progressively by greater ice and water thickness and by flight height, should it increase. Practical limitations

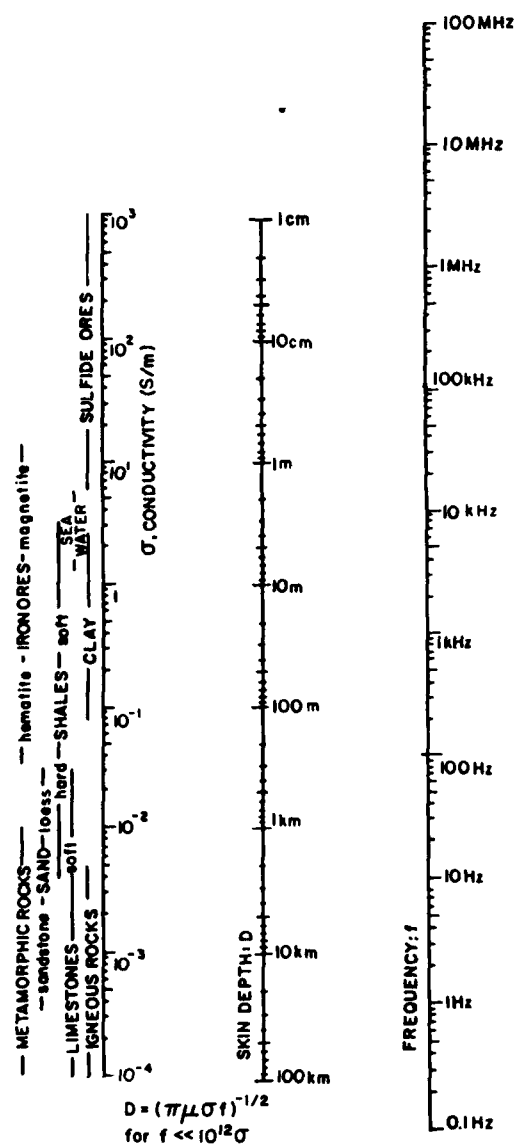


Figure 7. Nomogram for obtaining representative electromagnetic skin depth vs frequency and conductivity. (After Won 1980.)

on the frequencies used in the AEM bird therefore limit the maximum depth of water that can be interpreted at a given error level, as well as the maximum water depth at which the conductivity of the seafloor can be estimated. For practical purposes, and with error levels associated with the AEM system used, the error is less than 5% of the water depth down to one skin depth. The probable error in water depth for the AEM system used is ± 0.3 , ± 1.0 , and ± 2 m for water depths of 10, 15 and 20 m, respectively. As a general estimate the error is about 10% of the seawater depth at about 1.5 skin depths for the system used.

The electromagnetic skin depth, or the depth of penetration, is mainly determined by the AEM system frequency and the ground (seawater) conductivity. For most situations the skin depth D defines the limiting depth at which reasonable AEM sounding estimates can be made. The electromagnetic skin depth equals $\sqrt{2/\omega\mu\sigma} \cong 503 \sqrt{1/\sigma f}$. For seawater the sounding depth can be about 1.5 skin depths. The nomogram in Figure 7 gives the relationship between AEM system source frequency, ground conductivity and skin depth for a wide range of materials and sounding frequencies. For seawater the skin depth is better illustrated in Figure 8. Since Beaufort Sea water during the winter has a conductivity of about 2.5 S/m,

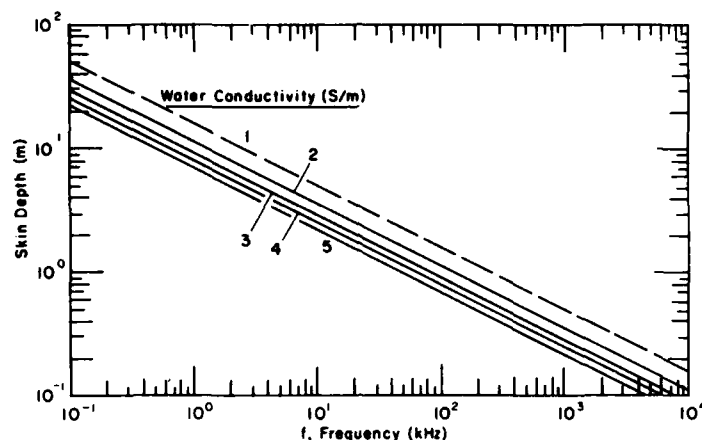


Figure 8. Electromagnetic skin depth in saline water vs antenna frequency and water conductivity.

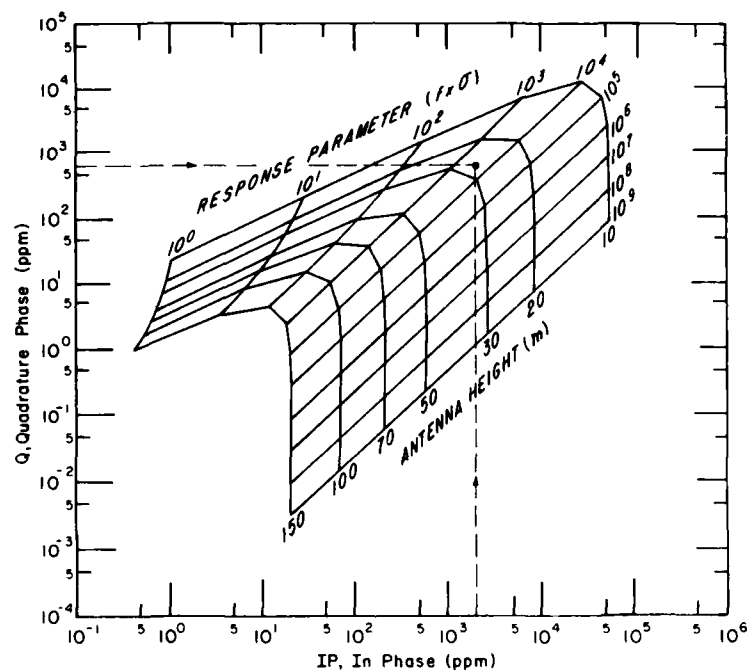


Figure 9. Example of an Argand diagram used for determining the AEM bird elevation above (and the apparent conductivity of) a conductive half-space. The diagram models the response of a horizontal coplanar coil pair, separated about 6.5 m.

the effective sounding depth of our AEM system at 527.5 Hz is between about 13.5 (1 skin depth) and 21 m (1.5 skin depth). The conductivity of the surface layer of Beaufort Sea water in summer will generally be lower because of melting of the sea ice canopy. Under this condition the AEM system sounding depth will be proportionately deeper.

With the aid of an Argand diagram (Fig. 9) formulated on the basis of a given T_x - R_x coil spacing and orientation, the height of the bird above the conductive surface and the apparent conductivity of the conductive layer can be estimated. For example, if the in-phase and

quadrature amplitudes at the receiver coil are 2000 and 850 ppm, respectively, then the intercept of the related lines in Figure 9 indicates that the bird is about 26 m above the conductor, or in our case the seawater, and that the response parameter is 5000. It follows that if the Tx coil was operating at a frequency of 2000 Hz, the apparent seawater conductivity would be $5000/2000 = 2.5$ S/m. Through appropriate multilayer analyses as outlined above, the depth to and conductivity of multiple conductive layers can be estimated.

Normally for AEM interpretation, three "layers" are considered in the inversion process: ice, water and bottom. The data collected in 1985 were not adequate to enable determination of ice and bottom sediment conductivity, so the parameters determined by inversion were ice thickness, water depth and water conductivity. Ice and sea bottom conductivities were empirically fixed at reasonable values based on preliminary data interpretations and on comparisons of these findings to available ground truth at specific sites. The conductivities for both the sea ice and the sediment, typically about 0.02 S/m, are very low compared to the seawater.

A reason for reducing the number of parameters interpreted is to increase the volume of EM data "available" for estimating the snow and ice thickness. For some interpretations the seawater conductivity was fixed at 2.5 or 2.6 S/m to observe the effect on the snow and ice thickness and water depth determinations. Of the examples given in this paper, only for line 6L7 was the seawater conductivity fixed. This helped reduce noise or scatter in the interpreted snow and ice thicknesses and water depths. Fixing the seawater conductivity at a reasonable value does not affect the snow and ice thickness determination very much since the highly conductive water yields a strong AEM response, which allows a good determination of snow and ice thickness even if the water conductivity used is not very accurate.

If system noise levels are 1 ppm, water conductivity and distance to a horizontal water surface should be estimated to about 1%. Sea ice thickness should be estimated to within a few percent for thick plate or level ice. However, because the laser profiler used had an accuracy on the order of ± 10 cm, ice thickness estimates will vary accordingly.

Ice conductivity may also be estimated but only with accuracy if the high-frequency coils operate well above the 32-kHz frequency available for this study. A 50-kHz frequency will be used in our 1987 field program. However, Liu and Becker (1987) indicated that an order of magnitude higher frequency may be needed to determine the conductivity of sea ice.

CALIBRATION OF AIRBORNE ELECTROMAGNETIC DATA

Typical AEM systems measure the amplitude of the secondary field at the receiver as a fraction of the primary field (from the transmitter) in parts per million (ppm). The phase of the measured signal can also be shifted relative to the transmitted field. The amount of this phase shift contains as much information as the overall amplitude of the signal. However, instead of measuring the amplitude and phase of the signal, the response is usually measured as the amplitude of each of the in-phase and out-of-phase (quadrature) signals.

Calibration and phasing of an AEM system consist of determining the size of these in-phase and quadrature responses from the actual voltages measured and recorded by the data acquisition system. Calibration thus yields a factor in parts per million (of the primary field at the receiver) per volt (ppm/V), which is later multiplied by incoming survey data (in volts) to obtain the correct response in ppm.

For the Prudhoe Bay survey, phasing and external calibrations were carried out on the ground using techniques which are standard for mineral exploration surveys. Phasing ensures that the signal used as a time reference in measuring phase shift has the correct phase itself. Once calibration and phasing have been completed, factors for both the in-phase and

quadrature data are determined by applying a known secondary field to the receiver and measuring the system response in volts.

However, this standard calibration technique for AEM data is not sufficiently accurate for the more stringent requirements of ice measurement or bathymetry. Therefore, calibrations had to be performed on a more empirical basis for this theory. Initially, forward models were computed to obtain theoretical in-phase and quadrature data at sites where the ice thickness and water depth and conductivity were "known." The model data (in ppm) were then compared to the real EM data (in ppm) measured at each ground truth site. Changes to the initial calibration factors were then made to yield an improved calibration. This technique is directly comparable to the use of a "bar check" for echo sounder calibrations. However, the use of ground truth for calibration restricts the accuracy of the AEM system results to the accuracy of the ground truth data. It also requires that ground truth be obtained on every survey, e.g. flying down a large unfrozen lead located in deep water. When a good calibration is obtained for an AEM system in the field, it has been found to remain very consistent from day to day.

Zero levels needed in the analysis of baseline drift removal (a practice common to a wide variety of high-resolution measurement techniques) are obtained by flying the system to an altitude of up to 500 m. At this elevation, there is no measurable response from the seawater. Zero level measurements were made before and after each flight line. Drift is normally assumed to be linear with time between these zeroing measurements, although in practice some nonlinearity is sometimes evident. It is thought that this drift is caused by small changes in the temperature of certain electronic components during a survey flight.

FIELD SURVEY

The AEM system flights were made over a variety of ice formations. These include first-year sea ice of several thicknesses and first- and second-year pressure ridges.

Newly formed lead

To assess system response and to aid in system calibration, a flight was made down the lead shown in Figure 10. The lead was in the process of freezing over. The near end of the



Figure 10. Skim ice on a newly formed lead profiled with the AEM system.

lead had about 1 cm of ice cover, while the far end was still open water. For our purposes, the lead represented a smooth, conductive water surface. Indeed, the AEM system responses indicated this by profiling a level surface over this feature. An average water conductivity of 2.8 S/m, about 10% too high, was also determined from the AEM data.

Refrozen lead

A profile made over a uniformly thick refrozen lead with a 3-cm snow cover (Fig. 11) is shown in Figure 12, and the data related to the profile are given in Table A1. The calibrated and drift-corrected AEM data for this profile are given in Figure 13. The profile in Figure 12 indicates a non-uniform lead ice thickness. This variation is not due to snow cover variations but is believed to be due to system noise and drift problems, to the poor accuracy of the laser profilometer, as previously mentioned, and to bird pitch and roll variations. The latter could not be fully accounted for in the bird pendulum data. Nevertheless, the average ice thickness

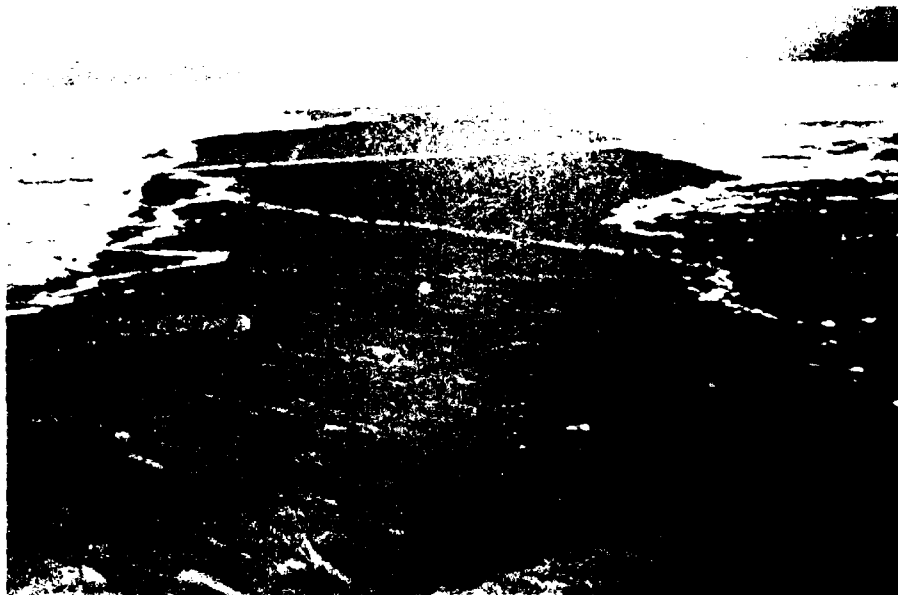


Figure 11. Refrozen lead profiled with the AEM system.

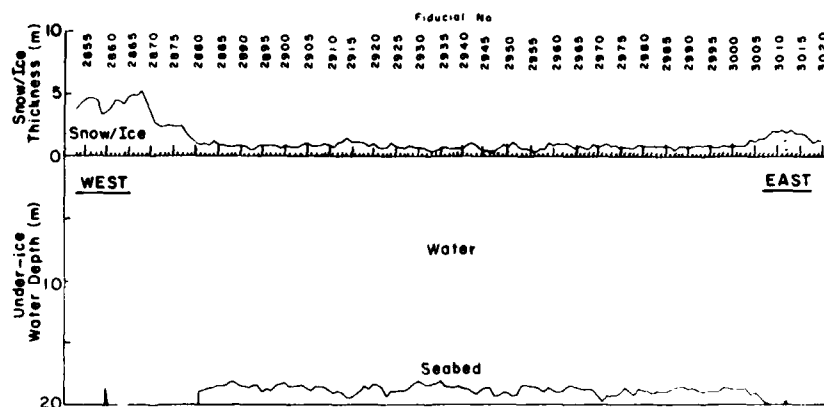


Figure 12. Snow and ice thickness and under-ice water depth for a flight over a refrozen lead located between about fid. no. 2880 and 3000.

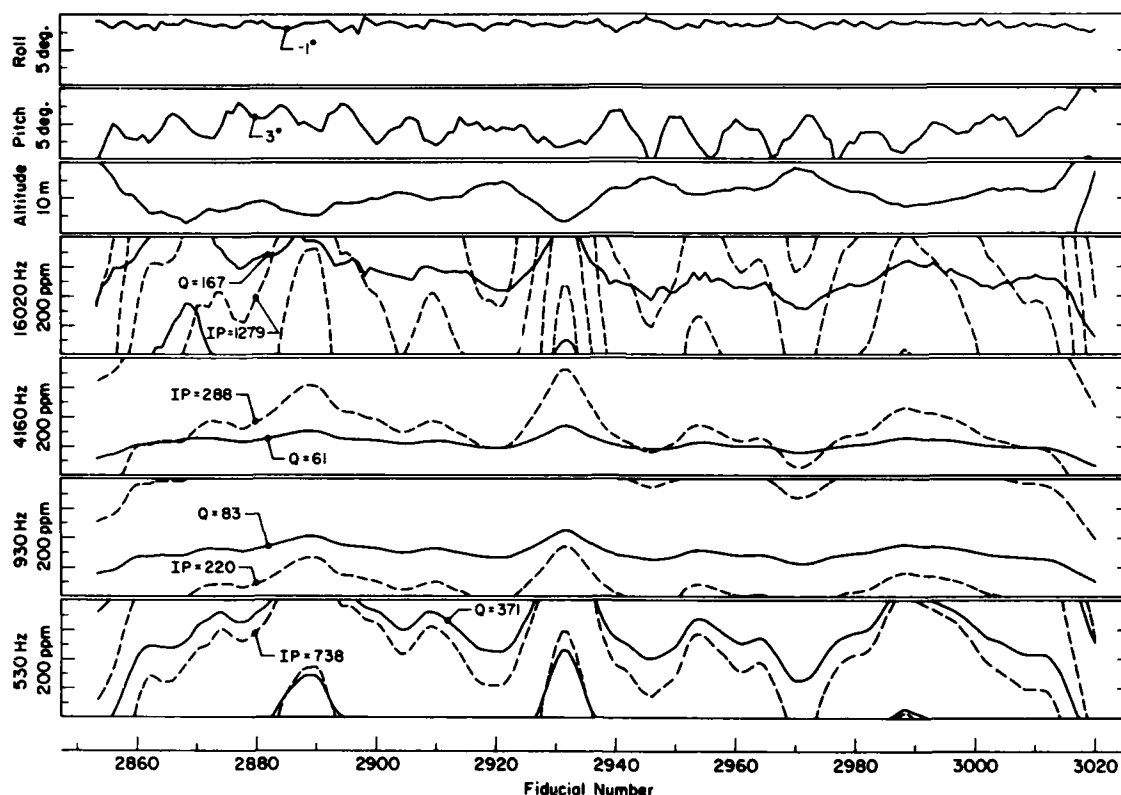


Figure 13. AEM, laser altimeter and altitude sensor data for flight over refrozen lead (Fig. 11 and 12). The graphs give the bird roll and pitch in degrees, the laser altitude in meters, and the 16,020-, 4160-, 930- and 530-Hz frequency coil in-phase (IP) and quadrature phase (Q) response in ppm.

for the profile, given in Table A1, is 0.80 m. This is remarkably close to the measured ice thickness of 0.75 m. This result is extremely encouraging and was achieved after significant improvements were made to the computer program to account for system noise and bird pitch and roll. The first analysis of the data gave a lower average ice thickness of 0.65 m (Kovacs et al. 1987). An improved vertical accelerometer and pitch and roll sensor, a reduction of system noise and a more accurate laser profilometer should further improve the profile results. The estimated seawater conductivity σ_w , listed in Table A1, varied from 2.35 to 2.49 S/m. The average was 2.45 S/m, which is in very good agreement with measured values of 2.5 S/m. Again, the first analysis of the data gave an average σ_w of 3.0 S/m, or about 0.5 S/m higher than the measured values. The seabed was also profiled at this site. This was not anticipated and therefore no direct sounding measurements were made to verify the AEM depth determinations. The variation in the bottom profile is not real, however, and is probably due to the factors discussed above.

Second-year floe

A second-year ice floe was selected for AEM profiling. The floe had a ridge extending from one side to the other. Survey lines were established on this floe by an Exxon research team. The lines were spaced 23 m apart, ran perpendicular to the ridge and were 250 m in length. We used two of these lines and ran a third line between them. This resulted in a test area 250 m long with three parallel lines about 11.5 m apart (Fig. 14). Along each line the snow and ice thickness was measured by drilling holes at about 7.5-m intervals except at the

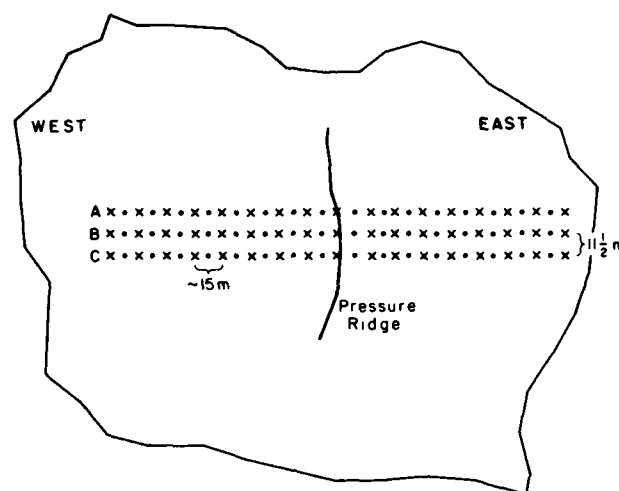


Figure 14. Grid layout on second-year sea ice floe, down which the AEM bird was flown.

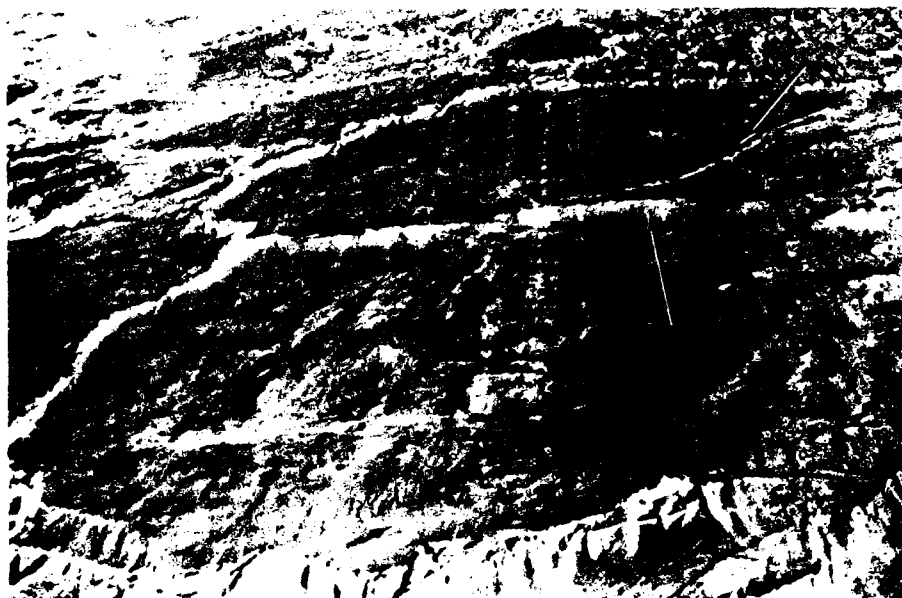


Figure 15. Aerial view of second-year sea ice flow and location of survey lines A, B and C.

ridge, where the spacing was about 3.75 m on lines A and B. At 30-m intervals along each line, we placed markers that could be seen from the air. Figure 15 is an aerial view, looking east, of the undulating floe relief, the ridge and the relative location of the three parallel lines. Two men can be seen standing on line A (near side of the ridge) and the person on the trail, arrow at upper right, gives a perspective of scale. The large dark object on the opposite side of the ridge is a 1.2-m-square, 2.2-m-high plastic building.

The snow and ice station thickness measured along each survey line is given in Table 1 and is shown graphically in Figure 16 along with the average snow and ice thickness for all three lines. The cross section of the ridge between stations 13 and 19 for each survey line is given in

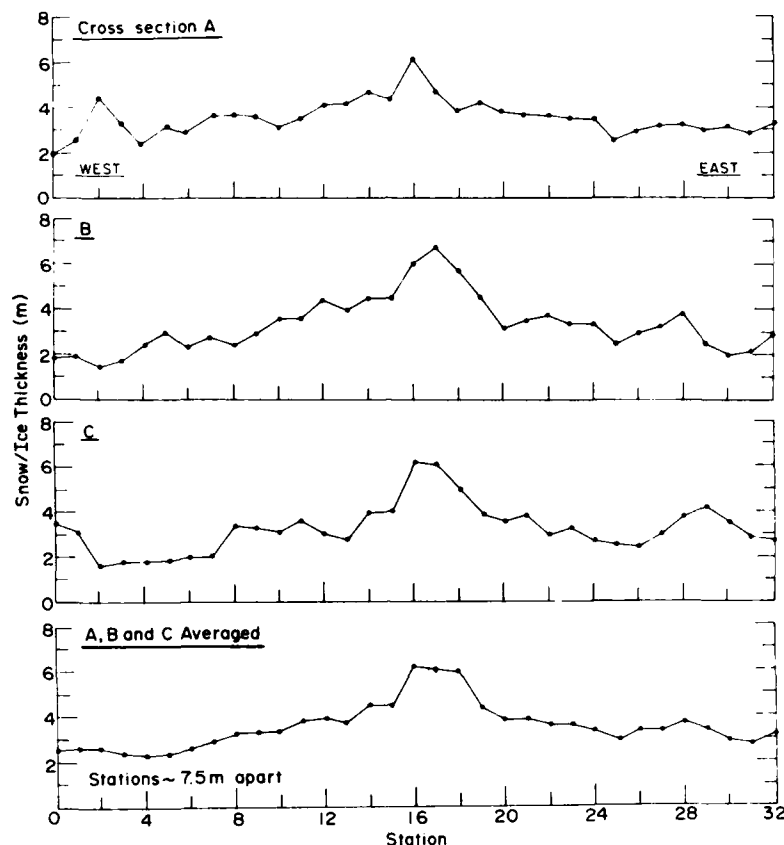


Figure 16. Snow and ice thickness along survey lines A, B and C, and average snow and ice thickness for the three lines.

Figure 17. The cross sections show that the ridge sail is just under 2 m high, the deepest part of the keel is offset from the center of the sail, the keel depth and geometry are different for each line, and the snow cover is thickest in the area of the ridge, which acts as a "snow fence." The snow and ice thickness profiles (Fig. 16) show, as expected, that variations in thickness exist between the profiles at the same station locations. Again, the thickest snow and ice was located at the ridge, which is situated between stations 15 and 17. The average snow and ice thickness for profiles A, B and C was 3.56, 3.58 and 3.74 m, respectively, for an overall average of 3.62 m.

The original intent was to fly the AEM bird down each survey line and note each ice surface station location on the data file as the bird passed over the marker. Then a comparison of the AEM ice thickness data to the drill hole data was to be made. This was not possible for reasons given below. Flights were made from west to east, nearly into the prevailing wind. The first flight pass quickly revealed that it would be extremely difficult to fly the bird, suspended 30 m below the helicopter, down such an exact linear course. Given this difficulty, an effort was made to fly the bird as close as possible down the center line of the three-line track.

The snow and ice thickness as obtained from two passes, flights 6L3 and 6L4, with the 16-kHz coil in the bird as shown in Figure 18. The thickness for three passes with the 32-kHz coil, flights 8L2, 8L3 and 8L4, is shown in Figure 19. The data associated with each flight are listed in Tables A3-A7.

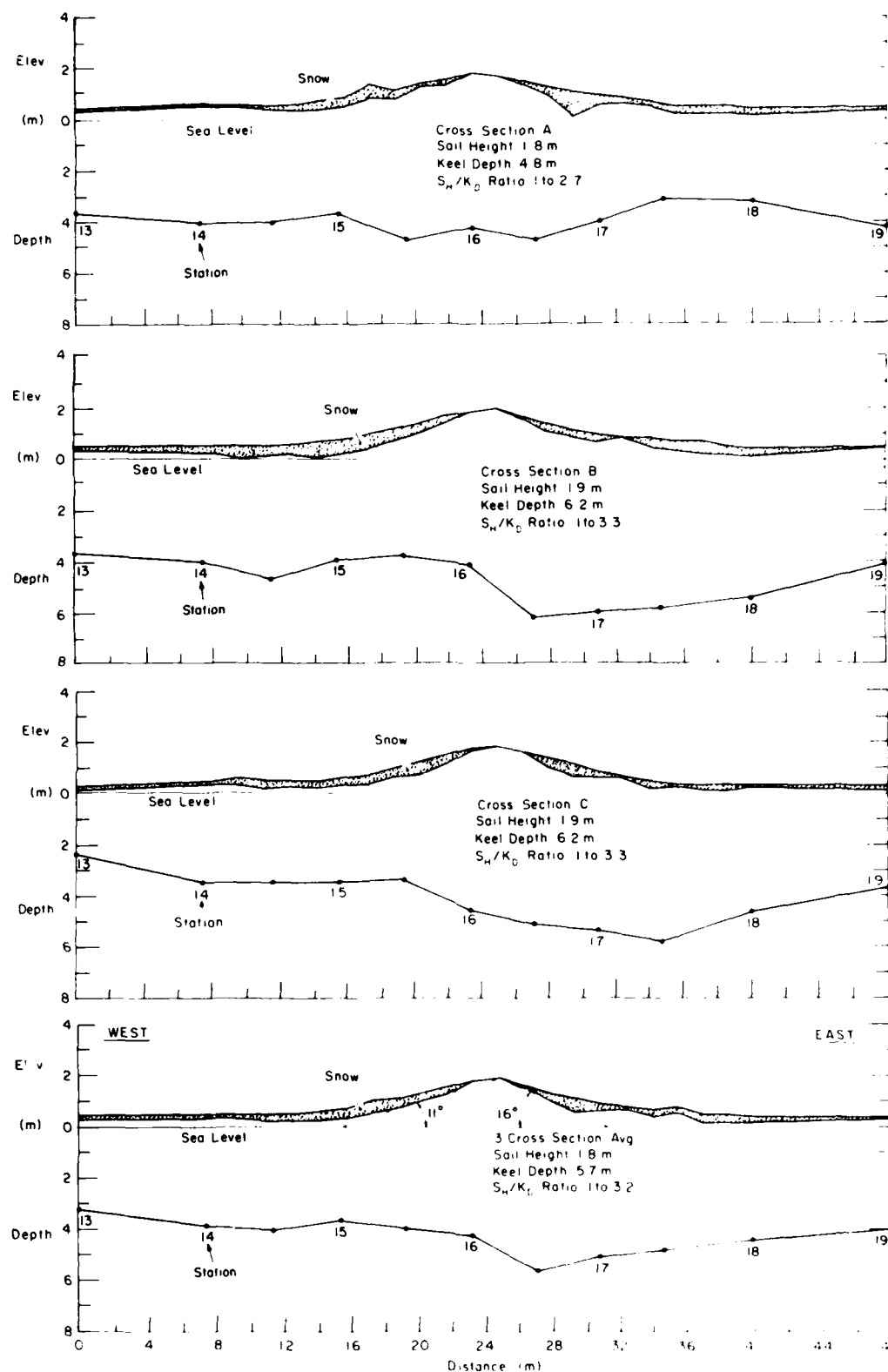


Figure 17. Cross section of second-year pressure ridge crossing survey lines A, B and C at about station 16.

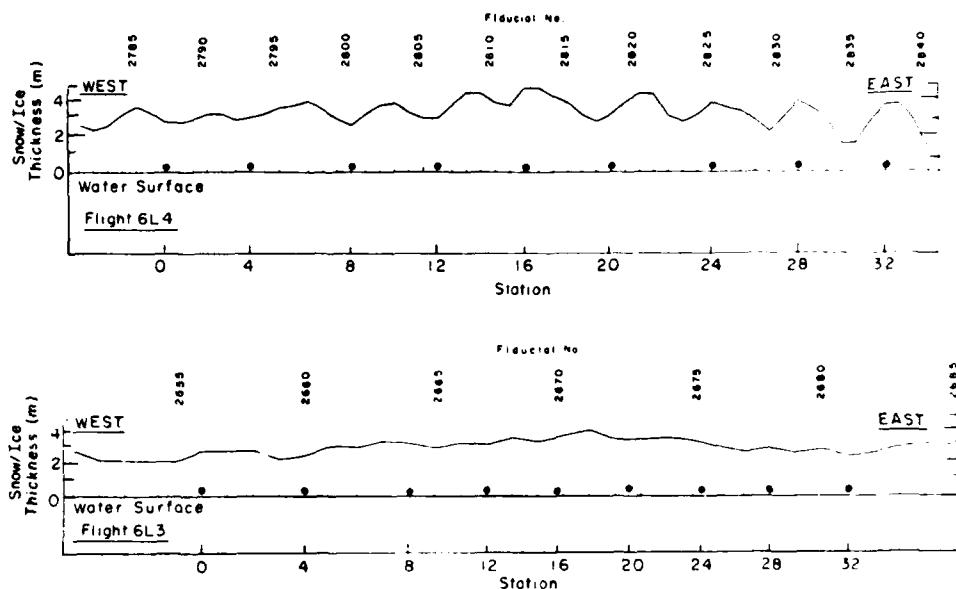


Figure 18. Snow and ice thickness obtained from flights 6L3 and 6L4 down the grid track on the second-year sea ice floe.

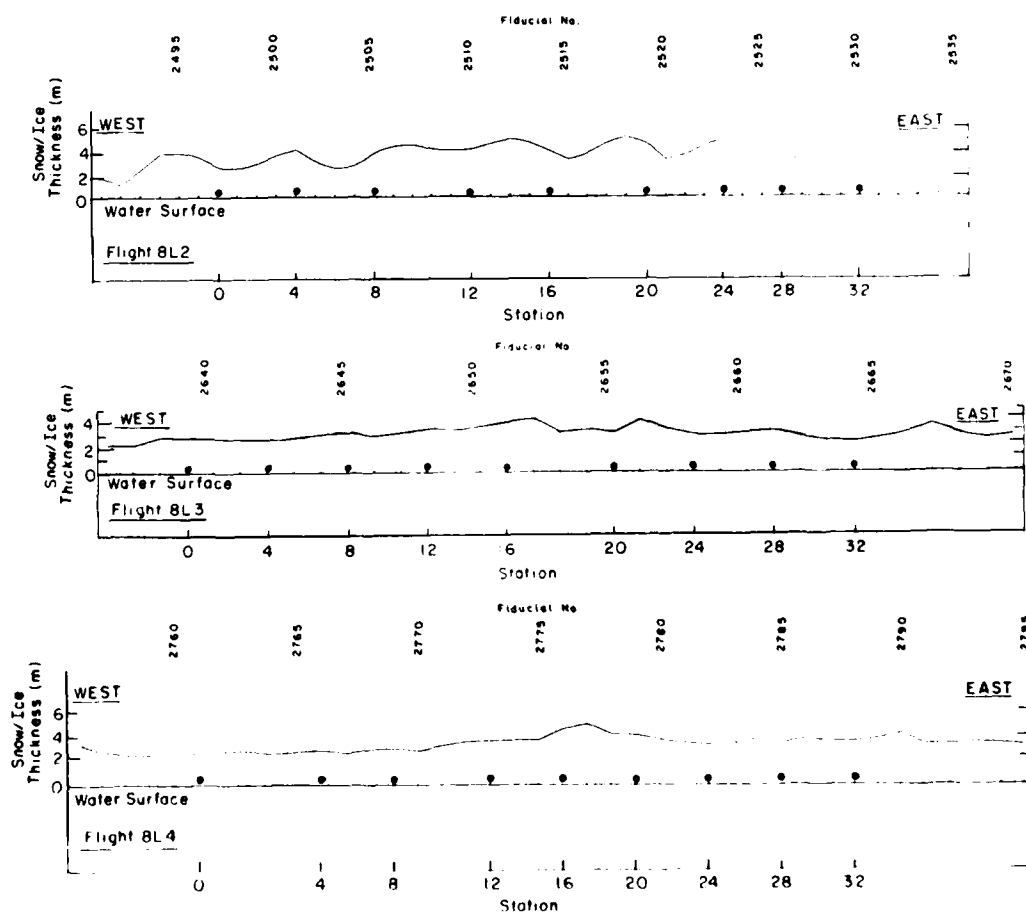


Figure 19. Snow and ice thickness obtained from flights 8L2, 8L3 and 8L4 down the grid track on the second-year sea ice floe.

Table 1. Average snow and ice thickness t_a and seawater conductivity σ_w for each flight over the second-year sea ice floe.

Flight no.	Avg. t_a (m)	Avg. σ_w (S/m)
8L2	4.07	2.59
8L3	3.07	2.35
8L4	3.55	2.46
6L3	3.20	2.48
6L4	3.45	2.47
Avg. all	3.47	2.47

Flight 6L4 was made at the lowest flight speed, during which 51 thickness measurements were made down the 250-m track. This was followed by flight 8L2, during which 34 thickness measurements were made. Flights 6L3, 8L3 and 8L4 were made at about the same speed, during which 26, 26 and 28 thickness measurements, respectively, were made.

Snow and ice thickness profiles from flights 6L4 and 8L2 (Fig. 18b and 19) show a waviness not at all characteristic of the measured thickness. During these two slow runs the bird was not stable. It moved from one side of the flight path to the other. The nose of the bird would turn slowly left and then move beneath the helicopter to the left side; then the nose would swing right,

and the bird would slide to the right like a pendulum. This movement could not be fully accounted for in the analysis of the data and is believed to be the cause of the undulations in the snow and ice thickness profile. The profiles obtained at the higher speed are more representative of the average measured snow and ice thickness profile in Figure 16 in that there is a gradual thickening of the ice in the area of the ridge. Nevertheless, the AEM profiles do not clearly reveal the ridge nor do they show the maximum ice thickness measured by drilling.

The AEM data do not show the thick ridge ice because of the large footprint and therefore the surface area over which the water surface was integrated into each AEM distance determination. Remember, the AEM system determines the distance from the bird to the water surface, which has depressions in it caused by ice bottom relief variations. Our preliminary assessment is that the AEM system footprint diameter is about 1.25 times the bird's height. This was determined by averaging the drill-hole-measured snow and ice thickness data over a window until the average thickness agreed with the AEM ice thickness interpretation at the center of the window. This footprint size has recently been verified by A. Becker and G. Liu,* who made an analysis similar to ours and obtained comparable results. Liu and Becker also made a worst-case assessment based on the expected current density on a flat, perfectly conducting, seawater interface, and then determined the relative area that would account for 90% of the observed secondary magnetic field. Their conclusion was that the footprint of an AEM system is about 1.4 times the bird height for a horizontal double-dipole coil system (with vertical coils). Therefore, the AEM distance to the ice/water interface is averaged over a relatively large area of undulating sea surface relief. This effect smooths out the snow and ice thickness variations in the drill-hole-measured thickness profile (Fig. 16).

Smoothing the snow and ice relief by the AEM system would clearly be of concern to those interested in detecting and measuring pressure ridge cross sections and depths. Nevertheless, this does not weaken the case for AEM measurement of snow and ice thickness. According to Becker and Liu, "it only strengthens the case for developing better methods of data interpretation." However, for measuring the mean snow and ice thickness of the arctic pack ice, AEM profiling should prove very useful. This may be examined in Table 1, which lists the average snow and ice thickness for each of the five flights down the track on the second-year ice floe, as well as the average seawater conductivity. The drill-hole measurements gave an average snow and ice thickness of 3.62 m for the three survey lines. The highest average AEM snow and ice thickness, 4.07 m, is for flight 8L2 and the lowest, 3.07 m, is for flight 8L3. These values are 12.4% higher and 15.2% lower than the average directly measured

* Personal communication, University of California at Berkeley.

value. From this analysis, the AEM system provided a representative mean snow and ice thickness to within about 15% of that measured by direct drilling.

Other factors may have affected the results. The difficulty of flying the AEM bird down the center of the track for which representative snow and ice thickness data existed was certainly one. Another problem is the three-dimensional form of the ice features. The 106 drill-hole measurements made along the track may not have been sufficient to fully define the mean ice thickness, and the algorithms used to interpret the AEM data were not refined enough to handle 3-D ice features (water depressions). The inversion technique is being improved, and the bird coil arrangement will be changed to allow better detectability and definition of the ridge keel/seawater interface.

The average seawater conductivities listed in Table 1 were in good agreement with the measured value of 2.5 S/m.

Grounded floeberg

In the early winter of 1983 a severe storm, with winds out of the southwest, hit the Beaufort Sea coast in the area of Prudhoe Bay, Alaska. The high winds broke up the sea ice over much of the continental shelf and drove this ice and the offshore pack ice westward. During this event, four deep-keeled "multi-year" ice floes became grounded on Cat Shoals. Sea ice floes driven against these anchor points failed. At first the ice piled on top of the grounded ice floes, adding weight and increasing their sliding resistance. The ice continued to break for some time. The ice rubble increased in height and then began to grow upwind. When the storm had driven the last of the first-year ice out to sea, four very large grounded ice formations remained. These features were about 0.5 to 0.75 km long and up to 100 m wide. The location of these formations on Cat Shoals, as determined by global navigation, is given in Figure 20. The bathymetric high points on Cat Shoals are typically less than 10 m below the surface, but shoaling to 8 m at one location is shown on one bathymetric chart of the area. Ice formation D seems to be grounded in waters deeper than 12 m, while formations A-C appear to have initiated at a grounding point in water 12 m or less in depth. The water depths at the southwest ends of formations A-D were measured by lead line and found to be 11.5, 11.6, 12.5 and 12.5 m, respectively. The two largest formations were B and C. These features each had an ice ridge over 15 m high (Fig. 21). Higher grounded sea ice rubble formations do occur. One that formed on a shoal about 23 km north of Oliktok Point was 22 m high (Fig. 22).

The four grounded ice formations on Cat Shoals did not break up or lose much ice by calving during the 1984 summer. Figure 23 shows the

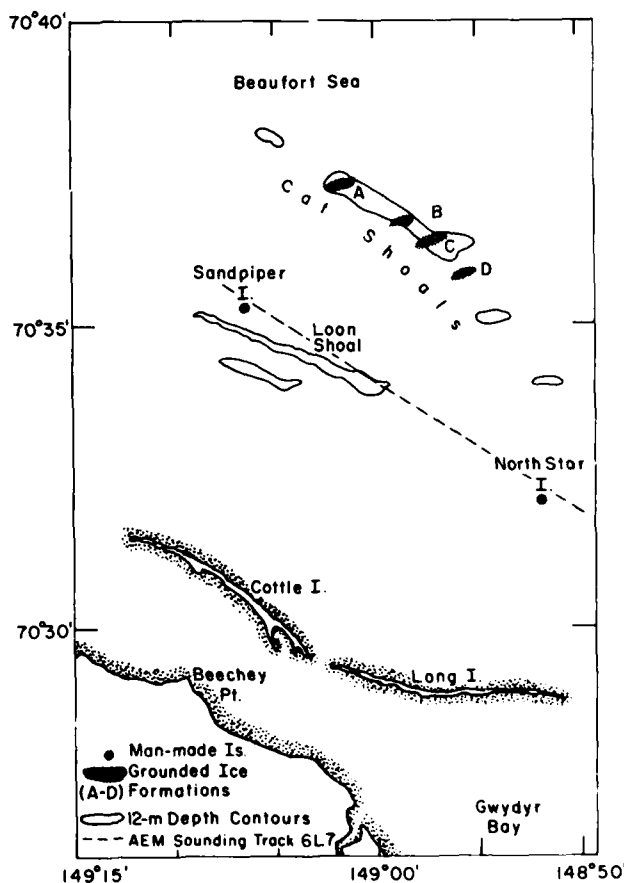


Figure 20. Location of grounded ice formations on Cat Shoals, and of Loon Shoal, Sandpiper and North Star islands, and AEM sounding track 6L7.

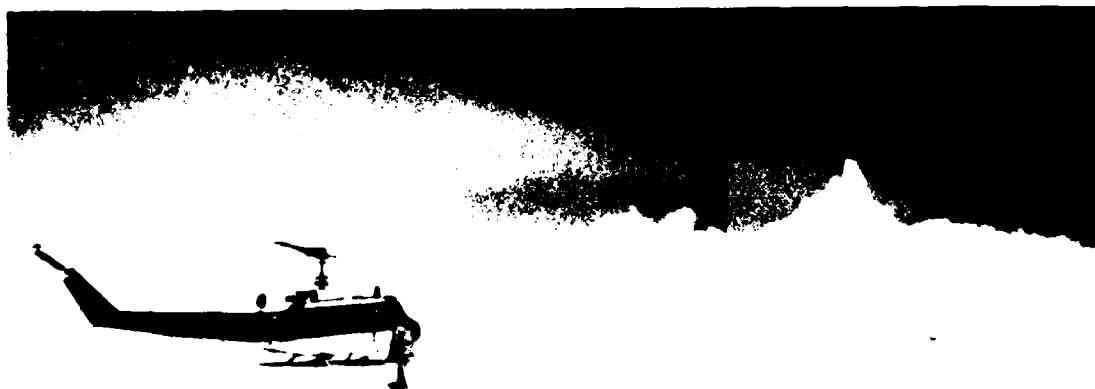


Figure 21. View of south side of grounded rubble formation C and its highest ridge.

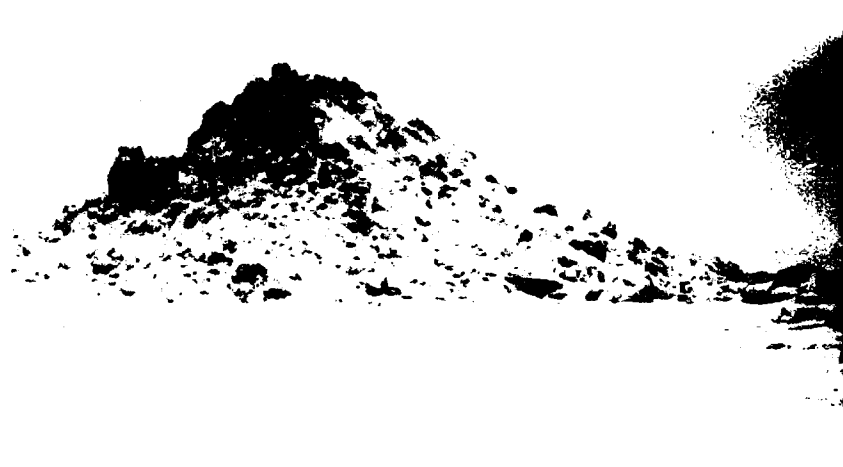


Figure 22. Extremely high (22 m) rubble formation found grounded in 1984 on a shoal north of Oliktok Pt., Harrison Bay, Alaska, at about 70°42.7'N, 149°44'W.

configuration of formations B, C and D in late August 1984, and Figure 24 shows the configuration of formations B and C on 27 March 1985. Having survived the summer melt season, these formations may now be referred to as grounded floebergs. At this time floeberg B was about 650 m long and 80 m wide, and floeberg C is some 600 m long and up to 90 m wide.

Stereo photography techniques were used to determine the topography of floeberg C along the parallel lines shown in Figure 25. The lines are 15 m apart. The highest point on the floeberg was about 13.5 m high on line 4 at the location of the circle. Figure 26 is a low-level aerial view of this high point, and Figure 27 is a view from the ice.

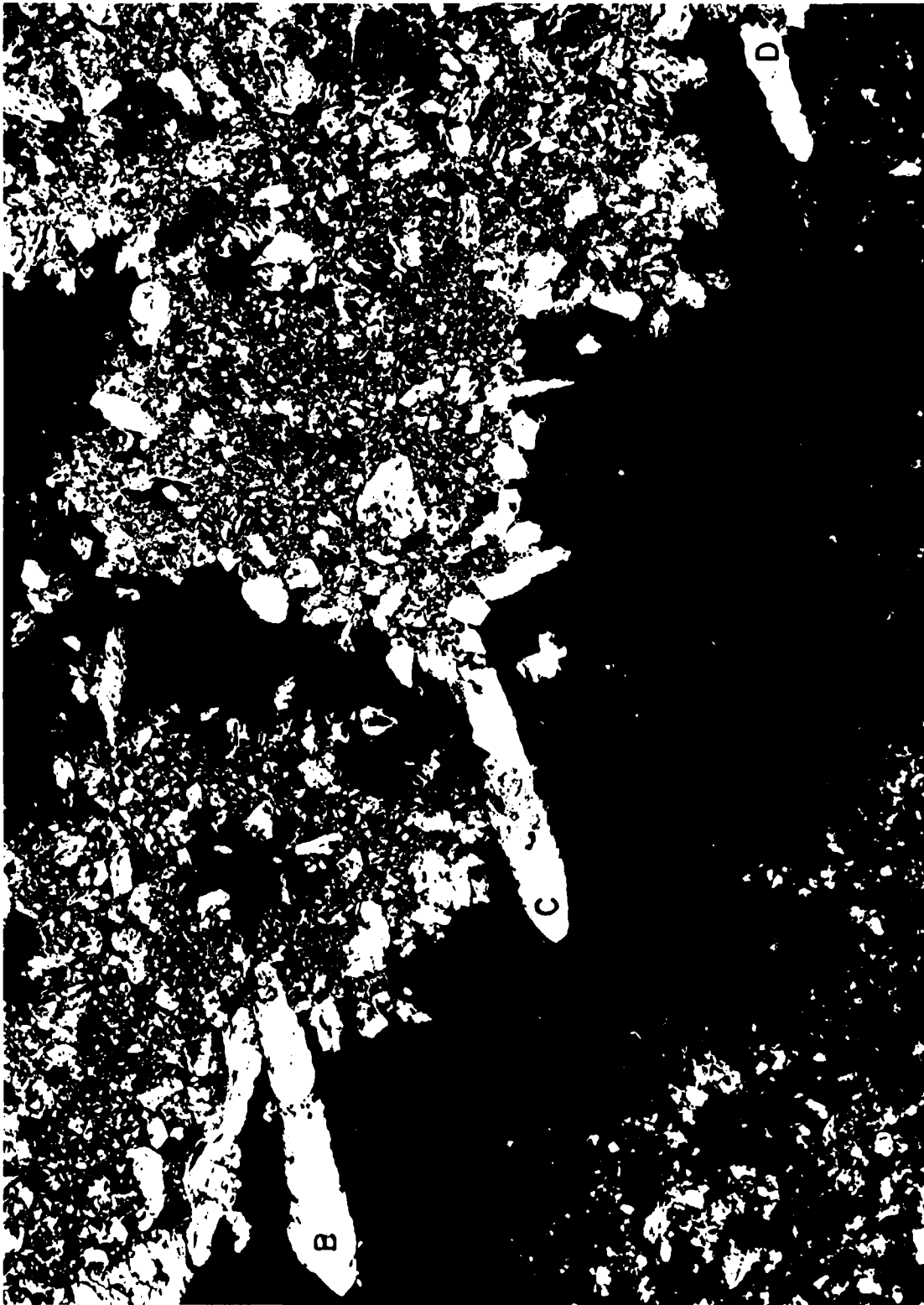


Figure 23. Aerial view of grounded rubble formations B, C and D in August 1984.



Figure 24. Aerial view of grounded rubble formations B and C in March 1985.

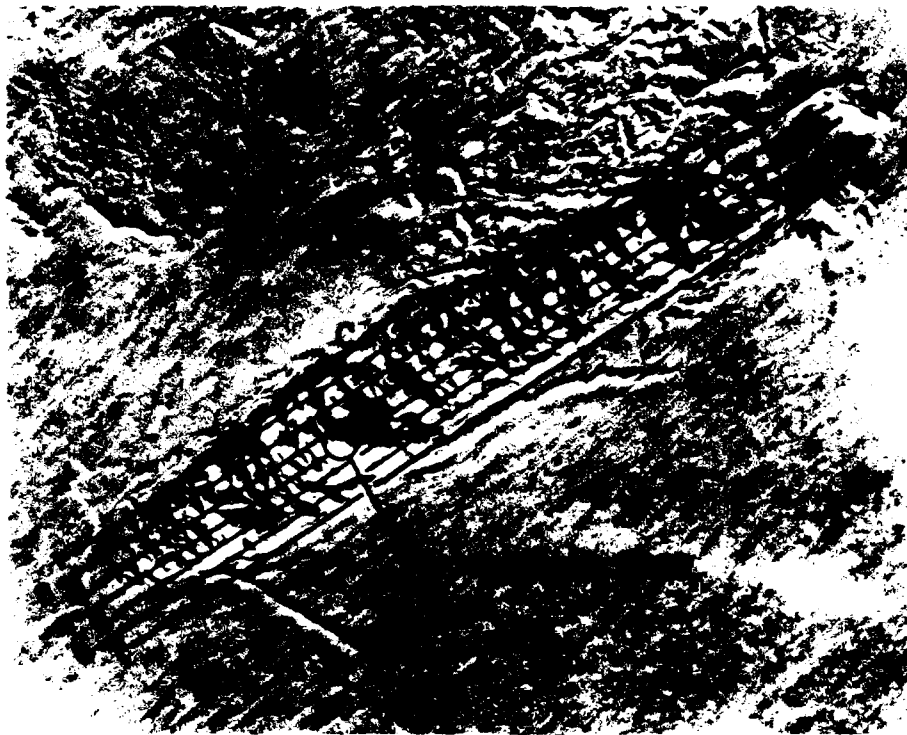


Figure 25. Floeberg C, showing the location of the highest ridge and the lines along which the topography was determined via stereo analysis.



Figure 26. Aerial view of floebergs B, C and D. The arrow points to the highest ridge on floeberg C.



Figure 27. North of floeberg C and its highest ridge. Note the vertical face where ice had calved off during the previous summer; this ice face is voidless.

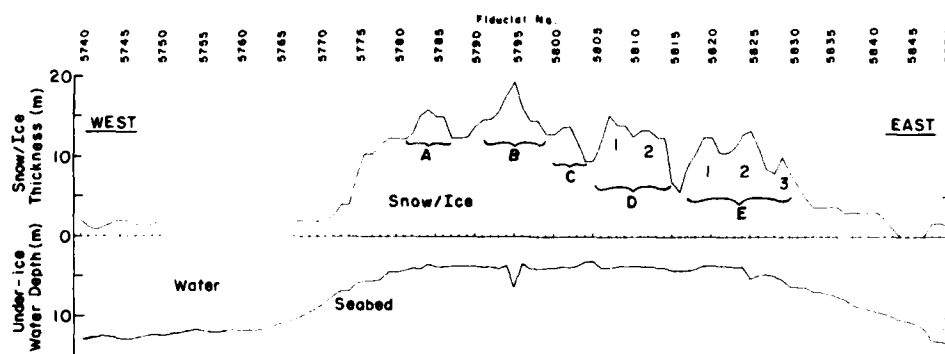


Figure 28. AEM profile results from the flight over floeberg C. Ridges A-E and numbered subpeaks correspond to similar features in Figure 29.

An AEM sounding run was made down each of the floebergs. The snow and ice thickness and under-ice water depth profiles for floeberg A were presented in Kovacs et al. (1987). Here we give AEM sounding results for floeberg C. The flight down floeberg C was made by lining up with the high point on the floeberg. This path would be nearly that along line 4. The AEM snow and ice thickness and under-ice water depth profiles are shown in Figure 28, and the tabulated data are given in Table A8 along with bird pitch, roll and flight elevation and seawater conductivity. The AEM results indicate there is an average of 4.8 m of water under the floeberg. This is not possible since the floeberg is solidly grounded on the shoal. The cause of this ambiguity is believed to be the existence of seawater within the submerged ice keel block structure. This is not unreasonable. The AEM system, because of the large footprint, may also have sensed the seawater off to the side of the floeberg. In addition, because the floeberg is three-dimensional, the layered model used in the data analysis may not have been adequate to define this imperfect transition between the ice block, the water and the seabed. Further refinement of the AEM data interpretation technique is progressing. A better solution to this apparent definition problem is anticipated.

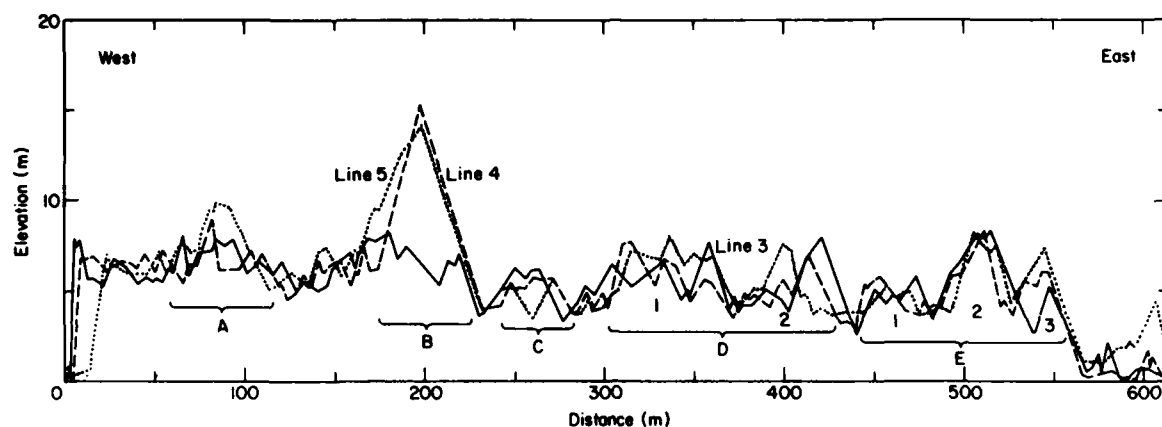


Figure 29. Snow and ice elevation profiles as determined by stereo analysis techniques along lines 3, 4 and 5 in Figure 25. Ridges A-E and numbered subpeaks correspond to similar features in Figure 28.

At about fiducial (fid.) no. 5760, the seawater depth was measured by lead line to be 12.5 m. The AEM data indicate about 11.7 m of water under the ice between fid. no. 5759 and 5761. The AEM snow and ice thickness was 1.5 m vs 1.62 m of ice and 0.2 m of snow measured by drilling. If the AEM snow and ice thickness includes 0.1 m of freeboard, then the AEM water depth at fid. no. 5760 is about $1.4 + 11.7 = 13.1$ m. This relative depth is within 10% of the measured value.

The airphoto-determined topography for lines 3, 4 and 5 (Fig. 25) is shown in Figure 29. These lines represent the corridor down which the AEM bird was flown. Note that the areas of rough topography indicated by letters and numbers in Figure 29 agree with similar peaks in Figure 28. The airphoto analysis gives an average snow and ice elevation for the three lines of 5.0 m. If we assume the floeberg is grounded in an average water depth of 11 m, then the ice keel should also be this deep. The average floeberg snow and ice thickness is then about $5.0 + 11 = 16$ m. The AEM data give an average floeberg snow and ice thickness of 12.4 m between fid. no. 5771 and 5840 and an average "water depth" of 4.8 m. For reasons previously discussed, the 4.8 m of water most likely represents seawater among the ice block keel structure, which is in contact with the seabed. This is further indicated by the very low conductivity for the "seawater" zone under the floeberg (Table A8). In short, the ice block and seawater conglomeration has affected the electromagnetic response, reducing the apparent conductivity below that of seawater but increasing the conductivity far above that of sea ice.

Since the water depth under the floeberg is essentially zero, the conductivity of the sediments forming the shoal takes on some importance. This is true in any area of very shallow water. Under this condition the sediments contribute significantly to the observed EM response. If the water is deeper than 1 skin depth, the sediments will have very little effect. However, for both floebergs and first-year pressure ridges, there is usually some water among the ice blocks. This conductive water will have an effect on the AEM response. In the absence of ground truth information on sediment conductivity, a fixed value was assumed, as discussed earlier.

In any event, if the average 4.8 m of "water" under the floeberg represents a porous ice block keel structure, the average AEM floeberg snow and ice thickness is $4.8 + 12.4 = 17.2$ m. This is 1.2 m thicker than the relative snow and ice thickness estimated with the use of the airphoto topographic results and assumed shoal depth.

Obviously a number of assumptions were made to generate the above averages. Nonetheless, the exercise is useful because it points up the need for further trials, improved data in-

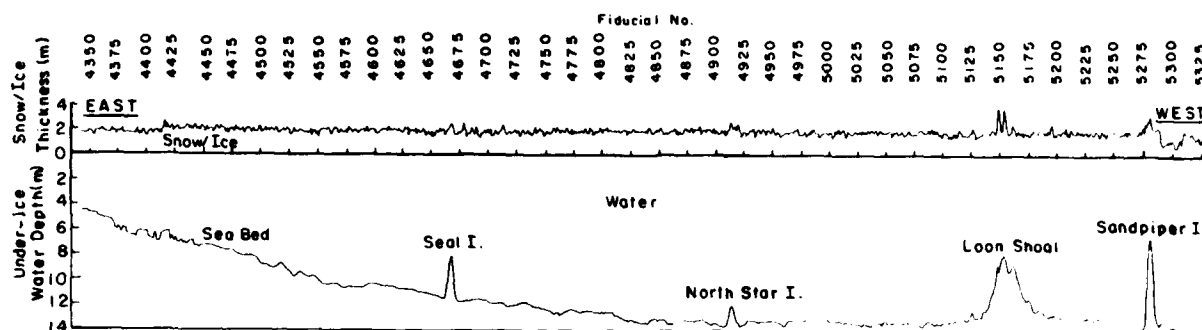


Figure 30. AEM profile results obtained from flight 6L7. A portion of this flight line is shown in Figure 20.

terpretation techniques and extensive ground truth measurements. For many situations the collection of ground truth will not be a significant problem. However, for ice features such as the floebergs, detailed ice thickness and water depth measurements would be extremely time consuming and prohibitively expensive. Under this situation certain approximations, such as those above, will have to suffice in assessing the profiling capability of the AEM system.

Flight line 6L7 began in shallow near-shore water and extended northwestward over the fast ice into deeper water. The location of a portion of this flight track is shown in Figure 20. Sandpiper and North Star islands are man-made gravel exploration islands. Sandpiper Island was built in 14.9 m of water and North Star in 13.7 m. To the southeast of Sandpiper Island the flight line passed another man-made structure, Seal Island, built in 11.9 m of water. Our flight line ran off the north side of the islands, where the water was about 0.5 m deeper. The relative water depths off Seal, Sandpiper and North Star islands were about 12.5, 14 and 15.5 m, respectively.

The AEM snow and ice thickness and under-ice water depth along track 6L7 are graphically presented in Figure 30. The nonpressured snow and ice thickness is seen to vary but averages 1.89 m thick between Seal and Sandpiper islands. The variations in the snow and ice relief are due to real snow and ice thickness variations as well as to system noise and drift problems and low laser accuracy. Nevertheless, the average AEM snow and ice thickness is in reasonable agreement with six drill hole measurements, which averaged 1.74 m.

The shoaling of the seabed at the location of the man-made islands (Fig. 30) is apparently due to the AEM system sensing the submerged slope of the gravel islands. The average under-ice water depth determined by AEM off Seal, Sandpiper and North Star islands was about 11.75, 13.25 and 14 m, respectively. Adding the average AEM snow and ice thickness (minus the freeboard) of about 1.75 m to these under-ice water depths gives relative water depths at each island of about 13.5, 15 and 15.75 m, respectively. Compared to the relative values given above, the AEM data overestimated the apparent water depth but by under 10%. This will be further evaluated in our next field program.

CONCLUDING REMARKS

The May 1985 field program was undertaken to determine the feasibility of using a multi-frequency airborne electromagnetic sounding system for measuring ice thickness. Funding and time constraints necessitated the use of a "standard" geophysical survey system and programs not fully developed for data interpretation. Nevertheless, the results proved encouraging in that reasonable measurements were made of both thick and thin first-year sea

ice as well as second-year ice of varying thicknesses. No other remote measurement system has demonstrated the capability of profiling such a variety of ice types and thicknesses. In addition to profiling sea ice thickness, information was obtained, for the first time from a remote sensor, on seawater conductivity and the depth of water under a sea ice cover.

For the next field program the AEM system is undergoing a major redesign. A new bird shell has been fabricated of Kevlar fabric. This shell will be about 0.35 m in diameter and 3.5 m long. The reduced shell size, along with new coil and electronic mounting platforms inside the bird and lighter coils, should reduce the weight of the bird to about half that of the bird used in 1985. The smaller bird will not only reduce shipping costs of the AEM system to remote areas but more importantly is a major first step to downsize the bird for deployment from a fixed-wing aircraft.

The new bird will have coils positioned to better define ice keels and their depth. Coil frequencies will be about 0.8, 4.5, and 50 or 60 kHz. The 0.8-kHz data should allow for profiling water depth to at least 10 m, and the 4.5-kHz data should provide water conductivity information. The high-frequency data will be used to obtain sea ice conductivity. Theoretical modeling indicates that resolution of sea ice conductivity to better than 0.1 S/m may be possible when sounding at 50 kHz, and there is a 1-ppm system precision. If the above sea ice conductivity determination proves successful, it would, in principle, be possible to determine the bulk porosity of the sea ice and infer its strength based upon the work of Kovacs et al. (1987). Reduction of system noise and drift are of paramount importance to the achievement of the desired level of precision in sea ice conductivity measurement.

Techniques for reducing system noise and drift have been investigated, and acceptable solutions will be implemented in the new AEM sea ice thickness measurement system. The dynamic range of the system will be increased about 32 times over that in the 1985 survey system. This increase will be achieved through the use of a 16-bit data acquisition system with a 20-V digitization window. Improvements to the calibration technique will be implemented and will include a new unique built-in absolute phasing and calibration technique. Calibration methods which can be applied at the postprocessing phase of data interpretation have also been developed, because standard airborne electromagnetic calibration techniques used for mineral exploration proved inadequate for sea ice thickness measurement. These changes should provide the first truly absolute measurements ever collected with an AEM system and include the capability to deal with negative, missing and saturated data, as well as the ability to recognize the best possible interpretation of the data.

A Micro VAX II computer has been obtained for the 1987 field study. This unit should vastly improve the speed of data interpretation. We expect a processing time of about 1 second per data point. An array processor for the computer is being considered for the future, and this addition should increase processing to at least 20 data points per second.

The 1985 AEM system had a sampling rate of 10 data points per second. The new ice measurement system should have a sampling rate of 20 data points per second. This rate provides for an ice thickness measurement about every 2.5 m at a flight speed of 100 knots. Therefore, with an array processor it should be possible for the computer to interpret AEM sea ice thickness data in real time when the data are collected at a sampling rate of 20 per second.

Future plans include shortening the AEM bird further to allow it to be deployable by an existing fixed-wing aircraft launcher system, using a digital receiver to replace the current analog signal processing system, developing a bird that generates a wideband time-domain signal, rather than the discrete continuous-wave coils now used, and including a global satellite positioning system to provide highly accurate flight track location information.

LITERATURE CITED

- Anonymous** (1968) Proposal for a feasibility study of an airborne technique for measuring sea ice thickness. Proposal submitted to U.S. Navy Oceanographic Office, Washington, D.C., by Geoscience Incorporated, Cambridge, Massachusetts.
- Becker, A., H. Morrison and K. Smits** (1983) Analysis of airborne electromagnetic systems for mapping thickness of sea ice. Naval Ocean Research and Development Activity, NORDA Technical Note 216.
- Fraser, D.C.** (1979) The multicoil II airborne electromagnetic system. *Geophysics*, **44**(8): 1367-1394.
- Fraser, D.C.** (1981) Magnetite mapping with a multicoil airborne electromagnetic system. *Geophysics*, **46**(11): 1579-1593.
- Ghosh, D.P.** (1971) The application of linear filter theory to direct interpretation of geoelectrical sounding measurements. *Geophysical Prospecting*, **19**: 192-217.
- Grant, F.S. and G.F. West** (1965) *Interpretation Theory in Applied Geophysics*. New York: McGraw-Hill.
- Holladay, J.S.** (1980) Interpretations of EM sounding data for a stratified earth by means of non-linear regression. Masters thesis, University of Toronto, Ontario, Canada.
- Jupp, D.L.B. and K. Vozoff** (1957) Stable interactive methods for the inversion of geophysical data. *Royal Astronomical Society Geophysical Journal*, **42**: 957-976.
- Kaufman, A.A. and G.V. Keller** (1983) *Frequency and Transient Soundings*. Amsterdam: Elsevier.
- Keller, G.V. and F.C. Frischknecht** (1986) *Electrical Methods in Geophysical Prospecting*. New York: Pergamon.
- Koefoed, O.** (1972) A note on the linear filter method of interpreting resistivity sounding data. *Geophysical Prospecting*, **20**: 403-405.
- Kovacs, A., R.M. Morey, G.F.N. Cox and N.C. Valteau** (1987) Modeling the electromagnetic property trends in sea ice. USA Cold Regions Research and Engineering Laboratory, CRREL Report 87-6.
- Lancosz, C.** (1961) *Linear Differential Operators*. London: Van Nostrand.
- Liu, G. and A. Becker** (1987) Determination of sea ice conductivity by airborne electromagnetics. University of California, Berkeley. Interim report to USA Cold Regions Research and Engineering Laboratory.
- Marquardt, D.W.** (1963) An algorithm for least squares estimation of nonlinear parameters. *Society for Industrial and Applied Mathematics Journal of Applied Mathematics*, **2**: 431-441.
- Morrison, H.F. and A. Becker** (1982) Analysis of airborne electromagnetic systems for mapping depth of sea water. University of California at Berkeley, Engineering Geoscience Report.
- Pemberton, R.H.** (1962) Airborne E.M. in review. *Geophysics*, **27**: 691-713.
- Verma, R.K.** (1982) Review of electromagnetic field calculations by digital linear filtering. *Radio Science*, **17**: 1067-1085.
- Walt, J.R.** (1951) The magnetic dipole over a horizontal stratified earth. *Canadian Journal of Physics*, **29**: 577-592.
- Ward, S.H.** (1970) Airborne electromagnetic methods. In *Mining and Groundwater Geophysics* (L.W. Morey, Ed.). Geological Survey of Canada, Economic Geology Report 26.
- Won, I.J.** (1980) A wide-band electromagnetic exploration method—Some theoretical and experimental results. *Geophysics*, **45**: 928-940.

APPENDIX A: FIELD SURVEY RESULTS

Table A1. Refrozen lead flight results.

Fiducial No.	AEM Bird			Ice Thick. (m)	Water Depth (m)	Water Conduct. (S/m)
	Pitch (Deg.)	Roll (Deg.)	Elev. (m)			
2900	1.5	-0.5	34.87	0.63	18.48	2.46
2901	1.3	-0.6	35.01	0.75	18.62	2.47
2902	1.9	-0.5	35.29	0.76	18.77	2.46
2903	2.1	-0.6	35.65	0.71	18.89	2.44
2904	2.2	-0.7	35.61	0.95	18.95	2.41
2905	2.9	-0.1	35.42	1.03	19.25	2.41
2906	2.9	-0.8	35.40	0.83	19.14	2.44
2907	2.6	-0.8	35.12	0.80	19.00	2.42
2908	1.3	-1.1	34.80	0.83	19.18	2.40
2909	1.2	-0.4	34.53	1.00	19.02	2.41
2910	0.9	-0.5	34.75	0.84	19.34	2.40
2911	1.2	-0.6	35.04	0.71	19.34	2.43
2912	1.8	-0.6	34.90	1.10	19.09	2.44
2913	1.9	-0.9	35.12	1.16	19.35	2.43
2914	3.0	-0.8	34.97	1.49	19.78	2.40
2915	2.4	-0.7	35.67	1.13	20.05	2.35
2916	2.4	-0.7	36.15	1.09	19.72	2.35
2917	2.6	-0.9	36.50	1.10	19.50	2.37
2918	2.0	-1.2	36.78	1.02	18.86	2.40
2919	2.3	-0.8	37.01	0.77	19.14	2.42
2920	1.9	-0.7	36.90	1.05	18.46	2.46
2921	2.2	-0.7	37.22	0.69	18.58	2.46
2922	2.1	-0.8	36.95	0.74	18.67	2.47
2923	2.0	-0.4	36.43	0.67	19.89	2.43
2924	2.4	-0.6	35.39	1.12	19.04	2.45
2925	2.2	-0.6	35.08	0.78	19.25	2.43
2926	1.5	-0.9	34.58	0.71	19.13	2.43
2927	1.1	-0.7	34.04	0.63	19.27	2.42
2928	1.6	-0.7	33.06	0.86	19.06	2.42
2929	1.2	-0.7	32.57	0.73	18.58	2.45
2930	0.8	-0.9	31.93	0.70	18.24	2.46
2931	0.8	-0.9	31.57	0.65	18.62	2.45
2932	1.0	-0.8	31.64	0.57	18.90	2.43
2933	1.1	-0.5	32.22	0.37	18.76	2.42
2934	1.3	-0.6	32.76	0.48	18.62	2.44
2935	1.0	-0.7	33.34	0.65	18.08	2.48
2936	1.5	-0.6	33.87	0.78	18.63	2.47
2937	1.9	-0.4	34.77	0.59	18.91	2.44
2938	2.5	-0.9	35.39	0.68	19.05	2.43
2939	3.3	-0.9	35.98	0.66	18.46	2.48
2940	3.4	-1.4	36.24	0.68	19.09	2.44
2941	3.4	-1.0	36.13	0.94	19.03	2.44
2942	2.5	-0.9	36.19	1.10	19.13	2.45
2943	1.9	-0.6	36.75	0.86	19.51	2.42
2944	1.5	-0.7	37.64	0.44	19.04	2.44
2945	0.7	-0.2	37.61	0.73	18.73	2.47
2946	-0.3	-0.5	37.99	0.47	18.55	2.49
2947	0.6	-0.5	37.68	0.43	19.84	2.43
2948	2.2	-0.6	37.13	0.71	19.57	2.42
2949	3.0	-0.9	36.70	0.99	19.07	2.45

Table A1 (cont'd). Refrozen lead flight results.

Fiducial No.	AEM Bird			Ice Thick. (m)	Water Depth (m)	Water Conduct. (S/m)
	Pitch (Deg.)	Roll (Deg.)	Elev. (m)			
2950	2.9	-1.1	36.66	0.75	19.19	2.46
2951	3.0	-1.0	35.65	1.16	19.53	2.45
2952	2.1	-0.7	35.39	0.82	19.25	2.47
2953	1.4	-0.9	35.36	0.60	18.63	2.46
2954	0.8	-1.0	35.28	0.67	18.29	2.49
2955	0.2	-0.4	35.55	0.45	18.86	2.44
2956	0.0	-0.6	35.92	0.35	18.63	2.47
2957	0.4	-0.7	35.84	0.62	18.96	2.45
2958	1.9	-0.5	36.06	0.57	19.18	2.45
2959	2.2	-0.9	35.86	1.11	18.68	2.47
2960	2.8	-0.7	36.31	0.86	19.09	2.46
2961	2.4	-0.9	36.23	1.04	19.28	2.44
2962	2.1	-0.7	36.28	0.91	19.14	2.45
2963	2.1	-0.9	35.95	1.13	18.59	2.47
2964	2.0	-0.9	36.18	0.82	18.41	2.49
2965	1.3	-0.7	36.50	0.65	18.83	2.45
2966	0.1	-0.7	36.76	0.86	18.83	2.46
2967	0.3	-0.2	37.52	0.66	19.03	2.45
2968	1.3	-0.6	38.37	0.58	18.64	2.48
2969	1.4	-0.7	38.60	0.99	19.02	2.45
2970	1.9	-0.5	39.18	0.75	19.25	2.47
2971	2.6	-0.7	38.88	0.88	19.77	2.46
2972	3.1	-0.8	38.58	1.02	19.21	2.48
2973	3.0	-1.1	38.49	0.81	19.35	2.46
2974	2.3	-0.9	37.73	0.90	19.53	2.44
2975	1.5	-0.7	37.46	0.62	19.10	2.45
2976	1.3	-0.6	36.81	0.78	18.56	2.48
2977	-0.3	-0.8	36.50	0.65	19.04	2.47
2978	0.6	-0.4	36.25	0.65	19.04	2.47
2979	1.2	-0.6	35.83	0.95	18.74	2.47
2980	1.1	-0.9	35.87	0.80	18.92	2.47
2981	1.9	-0.5	35.76	0.80	18.92	2.47
2982	1.9	-0.7	35.68	0.75	19.38	2.45
2983	1.9	-1.0	35.35	0.83	19.01	2.46
2984	1.9	-1.0	34.90	0.84	19.10	2.46
2985	1.5	-0.7	34.41	0.84	19.15	2.45
2986	0.7	-0.5	34.12	0.78	18.90	2.46
2987	0.5	-0.7	34.25	0.47	18.77	2.46
2988	0.4	-0.7	33.76	0.81	18.74	2.45
2989	1.0	-0.7	33.85	0.80	18.65	2.46
2990	1.2	-0.5	34.06	0.68	18.90	2.46
2991	1.5	-0.6	34.04	0.81	18.74	2.47
2992	2.1	-0.7	34.04	0.86	19.04	2.46
2993	2.6	-0.7	34.10	0.85	19.32	2.44
2994	2.5	-0.7	34.18	0.90	19.15	2.45
2995	2.3	-0.8	34.44	0.80	18.92	2.47
2996	2.0	-0.6	34.63	0.68	19.25	2.44
2997	1.7	-0.6	34.78	0.72	18.99	2.46
2998	1.9	-0.9	34.91	0.90	18.66	2.47
2999	1.9	-0.7	35.29	0.76	18.83	2.46
3000	2.5	-0.8	35.46	0.84	18.82	2.47

Table A2. Survey line station drill-hole-measured snow and ice thicknesses.

Sta No.	Snow Depth (cm)	Ice Thickness (m)	Total Snow and Ice Thickness (m)	Sta No.	Snow Depth (cm)	Ice Thickness (m)	Total Snow and Ice Thickness (m)
a. Survey line A station.							
0	7	1.78	1.85	15	43	4.12	4.55
1	20	1.80	2.00	16	4	6.06	6.10
2	42	1.28	1.70	17	40	4.55	4.95
3	27	1.58	1.85	18	42	3.38	3.80
4	20	2.25	2.45	19	9	4.21	4.30
5	8	2.97	3.05	20	3	3.77	3.80
6	36	2.12	2.50	21	8	3.62	3.70
7	40	2.50	2.90	22	7	3.63	3.70
8	17	2.31	2.50	23	5	3.45	3.50
9	25	2.75	3.00	24	9	3.41	3.50
10	10	3.50	3.60	25	26	2.34	2.60
11	38	3.62	4.00	26	6	2.94	3.00
12	8	4.37	4.45	27	12	3.13	3.25
13	7	3.93	4.00	28	7	3.18	3.25
14	28	4.32	4.60	29	11	2.94	3.05
14.5	40	4.80	5.20	30	8	3.07	3.15
15	50	4.20	4.70	31	11	2.79	2.90
15.5	46	4.59	5.05	32	7	3.23	3.30
16	10	5.95	6.05	c. Survey line C station.			
16.5	5	7.65	7.70	0	20	3.40	3.60
17	29	6.61	6.90	1	8	3.19	3.27
17.5	31	6.29	6.60	2	10	1.60	1.70
18	21	5.59	5.80	3	5	1.70	1.75
19	9	4.51	4.60	4	10	1.75	1.85
20	28	3.07	3.35	5	33	1.70	2.03
21	9	3.51	3.60	6	30	1.86	2.16
22	8	3.67	3.75	7	18	1.97	2.15
23	47	3.13	3.60	8	10	3.30	3.40
24	41	2.99	3.40	9	7	3.23	3.30
25	41	2.99	3.40	10	6	3.14	3.20
26	5	3.25	3.30	11	8	3.57	3.65
27	23	3.07	3.30	12	13	2.97	3.10
28	8	3.82	3.90	13	12	2.73	2.85
29	22	2.43	2.65	14	13	3.87	4.00
30	5	1.95	2.00	15	27	3.83	4.10
31	24	2.06	2.30	15.5	52	3.93	4.45
32	9	2.81	2.90	16	10	6.20	6.30
b. Survey line B station.				16.5	30	6.35	6.65
0	9	1.91	2.00	17	21	5.99	6.20
1	10	2.50	2.60	17.5	15	6.05	6.20
2	12	4.43	4.55	18	21	4.84	5.05
3	48	3.02	3.50	19	24	3.76	4.00
4	18	2.27	2.45	20	55	3.30	3.85
5	4	2.06	2.10	21	6	3.79	3.85
6	39	2.71	3.10	22	34	2.76	3.10
7	18	3.52	3.70	23	11	3.19	3.30
8	7	3.63	3.70	24	20	2.55	2.75
9	7	3.58	3.65	25	39	2.31	2.70
10	22	2.98	3.20	26	8	3.42	3.50
11	20	3.40	3.60	27	43	2.77	3.20
12	9	4.11	4.20	28	9	3.71	3.80
13	10	4.10	4.20	29	9	4.16	4.25
14	6	4.64	4.70	30	9	3.41	3.50
				31	15	2.85	3.00
				32	38	2.72	3.10

Table A3. Line 6L3 flight results.

Fiducial No.	AEM Bird		Elev. (m)	Snow-ice Thickness (m)	Water Conduct. (S/m)
	Pitch (Deg.)	Roll (Deg.)			
2656	5.4	-0.3	39.98	2.82	2.49
2657	5.8	-0.5	39.17	2.85	2.42
2658	6.0	-0.8	38.85	2.92	2.51
2659	6.6	-1.1	39.08	2.29	2.42
2660	6.4	-1.2	38.77	2.53	2.42
2661	5.6	-1.2	37.76	3.17	2.46
2662	5.4	-1.3	37.07	3.08	2.45
2663	5.4	-1.2	36.45	3.52	2.51
2664	5.4	-1.1	36.66	3.35	2.48
2665	5.4	-0.7	37.06	3.13	2.56
2666	5.4	-0.6	36.29	3.42	2.51
2667	5.4	-0.6	35.76	3.29	2.50
2668	5.5	-0.7	34.80	3.76	2.52
2669	6.1	-0.9	35.02	3.47	2.48
2670	6.3	-0.8	35.11	3.90	2.56
2671	6.7	-1.0	35.20	4.24	2.56
2672	6.4	-1.2	35.76	3.58	2.48
2673	5.8	-1.1	35.39	3.60	2.51
2674	5.7	-1.2	34.90	3.75	2.55
2675	5.8	-1.3	34.98	3.52	2.50
2676	6.1	-1.2	35.65	3.08	2.46
2677	6.2	-0.8	36.12	2.75	2.43
2678	6.2	-1.0	36.05	3.01	2.43
2679	6.1	-0.6	36.65	2.72	2.46
2680	6.1	-0.7	37.30	2.92	2.42
2681	6.4	-0.8	39.12	2.44	2.42

Table A4. Line 6L4 flight results.

Fiducial No.	AEM Bird		Elev. (m)	Snow-ice Thick. (m)	Water Conduct. (S/m)
	Pitch (Deg.)	Roll (Deg.)			
2787	7.0	-1.1	38.92	2.84	2.44
2788	7.8	-0.8	39.53	2.85	2.54
2789	7.3	-0.5	39.63	3.04	2.57
2790	5.5	-0.5	38.98	3.25	2.42
2791	5.2	-0.2	38.54	3.25	2.42
2792	6.0	-0.4	38.55	2.88	2.40
2793	7.2	-0.9	38.53	3.05	2.40
2794	7.6	-1.1	38.54	3.26	2.38
2795	7.1	-1.2	37.99	3.61	2.38
2796	6.1	-1.2	37.13	3.77	2.44
2797	5.6	-1.4	36.00	4.01	2.48
2798	6.0	-1.4	35.93	3.57	2.47
2799	7.3	-1.1	36.49	2.97	2.45
2800	7.0	-0.7	36.89	2.58	2.40
2801	6.1	-0.5	35.60	3.28	2.42
2802	5.1	-0.3	33.95	3.76	2.39
2803	5.2	-0.3	33.17	3.90	2.43
2804	6.7	-0.9	33.81	3.32	2.43
2805	7.3	-1.1	34.68	3.00	2.40
2806	8.2	-1.7	34.62	3.01	2.41
2807	6.5	-1.4	33.24	3.80	2.45
2808	5.2	-1.5	31.69	4.53	2.50
2809	6.8	-1.5	30.98	4.54	2.60
2810	7.0	-1.2	31.95	4.02	2.63
2811	7.7	-0.7	32.98	3.82	2.60
2812	6.9	-0.4	32.32	4.87	2.62
2813	5.2	-0.3	31.99	4.79	2.55
2814	4.9	-0.1	31.92	4.32	2.53
2815	5.4	-0.4	32.56	4.02	2.56
2816	7.3	-1.0	34.18	3.27	2.54
2817	8.2	-1.7	35.22	2.84	2.46
2818	8.6	-2.1	34.54	3.25	2.47
2819	6.2	-2.0	32.98	3.98	2.49
2820	4.2	-1.4	31.51	4.49	2.52
2821	5.1	-1.3	30.91	4.46	2.57
2822	6.9	-1.0	32.10	3.20	2.52
2823	7.7	-0.1	32.56	2.88	2.52
2824	7.0	0.1	31.62	3.23	2.47
2825	4.4	-0.3	30.15	3.93	2.47
2826	3.9	-0.3	29.67	3.63	2.47
2827	5.6	-0.7	29.78	3.51	2.52
2828	7.7	-1.6	30.86	2.98	2.52
2829	8.1	-2.1	32.09	2.28	2.48
2830	6.5	-2.1	31.24	3.07	2.44
2831	4.5	-1.5	29.74	4.03	2.47
2833	6.8	-1.5	30.75	3.02	2.49
2834	7.8	-0.9	33.75	1.51	2.39
2835	7.6	-0.4	35.05	1.52	2.35
2836	6.0	-0.1	33.87	2.79	2.34
2837	4.2	-0.3	32.46	3.67	2.34

Table A5. Line 8L2 flight results.

Fiducial No.	AEM Bird			Snow-ice Thickness (m)	Water Conduct. (S/m)
	Pitch (Deg.)	Roll (Deg.)	Elev. (m)		
2497	5.7	-0.3	45.76	2.93	2.52
2498	5.9	-0.7	45.99	2.58	2.39
2499	3.8	-1.0	44.13	2.90	2.27
2500	3.1	-1.5	40.87	4.67	2.29
2501	3.4	-1.5	39.18	4.13	2.44
2502	4.0	-1.0	40.52	3.04	2.45
2503	5.0	-0.3	42.12	2.47	2.45
2504	5.3	0.2	42.29	2.71	2.44
2505	4.9	0.3	40.56	3.88	2.46
2506	4.2	0.0	38.96	4.55	2.54
2507	4.9	0.2	38.48	4.77	2.63
2508	6.0	0.1	39.27	4.20	2.58
2509	7.2	-0.5	40.01	4.09	2.54
2510	7.0	-0.5	40.08	4.18	2.52
2511	5.9	-0.7	39.23	4.74	2.57
2512	5.4	-1.2	38.48	5.15	2.60
2513	5.8	-1.1	39.45	4.81	2.55
2514	6.3	-0.9	41.89	4.01	2.45
2515	6.1	-0.2	43.98	3.24	2.41
2516	4.8	0.0	43.67	3.83	2.51
2517	4.5	0.1	42.20	4.90	2.66
2518	5.0	0.2	41.76	5.55	2.87
2519	6.1	-0.1	43.54	5.06	2.98
2520	7.7	-0.5	45.99	3.44	2.76
2521	7.9	-0.8	45.79	3.77	2.72
2522	5.6	-0.9	44.00	4.62	2.63
2523	4.7	-1.3	41.95	5.15	2.63
2524	4.7	-1.3	41.62	4.94	2.66
2525	5.1	-0.9	43.96	3.74	2.64
2526	4.5	0.0	46.56	2.79	2.67
2527	4.0	0.2	45.96	3.73	2.71
2528	4.0	0.2	43.87	4.73	2.72
2529	4.6	-0.1	43.48	4.97	2.87
2530	5.5	0.0	44.19	5.13	2.87

Table A6. Line 8L3 flight results.

Fiducial No.	AEM Bird		Elev. (m)	Snow-ice Thickness (m)	Water Conduct. (S/m)
	Pitch (Deg.)	Roll (Deg.)			
2639	5.2	-0.7	37.55	2.78	2.46
2640	5.7	-0.8	37.93	2.77	2.45
2641	5.7	-0.9	38.68	2.65	2.43
2642	5.7	-0.4	39.04	2.60	2.38
2643	5.7	-0.3	38.69	2.70	2.30
2644	5.6	0.1	37.67	3.00	2.23
2645	5.7	-0.1	37.00	3.13	2.26
2646	5.3	-0.1	37.34	2.78	2.24
2647	5.1	-0.4	37.31	3.23	2.39
2648	4.4	-0.7	37.12	3.52	2.44
2649	3.4	-0.8	36.83	3.34	2.33
2650	2.8	-0.6	36.05	3.57	2.23
2651	3.8	-0.9	35.52	3.95	2.14
2652	5.3	-0.8	35.69	4.08	2.10
2653	6.5	-0.7	37.24	2.96	2.03
2654	5.9	-0.3	37.51	3.28	2.05
2655	5.4	0.2	37.66	2.96	2.10
2656	4.8	0.2	36.26	4.02	2.11
2657	4.4	0.0	36.85	3.26	2.16
2658	4.0	-0.6	37.20	2.83	2.22
2659	3.8	-0.8	36.91	2.80	2.18
2660	3.4	-1.1	35.93	3.12	2.21
2661	2.9	-0.9	35.09	3.26	2.23
2662	3.8	-0.7	35.44	2.65	2.19
2663	5.1	-0.7	36.28	2.26	2.13
2664	5.5	-0.4	36.74	2.23	2.11

Table A7. Line 8L4 flight results.

Fiducial No.	AEM Bird			Snow-ice Thickness (m)	Water Conduct. (S/m)
	Pitch (Deg.)	Roll (Deg.)	Elev. (m)		
2761	5.9	-0.5	28.20	2.71	2.47
2762	5.6	-0.2	28.32	2.91	2.44
2763	5.2	-0.2	28.82	2.87	2.40
2764	5.3	-0.6	29.64	2.59	2.38
2765	6.6	-0.6	29.75	2.80	2.42
2766	6.1	-0.8	29.62	2.93	2.41
2767	6.6	-0.8	29.73	2.67	2.41
2768	5.8	-0.8	29.53	3.01	2.39
2769	5.9	-0.7	29.64	3.10	2.40
2770	5.3	-0.5	30.20	2.84	2.40
2771	5.2	-0.4	29.87	3.38	2.42
2772	5.4	-0.3	29.63	3.78	2.45
2773	5.3	-0.4	29.83	3.78	2.45
2774	5.7	-0.3	29.98	3.88	2.44
2775	5.5	-0.4	30.34	3.84	2.45
2776	5.5	-0.6	29.40	4.89	2.54
2777	5.2	-0.8	28.63	5.34	2.59
2778	4.7	-0.8	29.04	4.39	2.53
2779	4.4	-0.7	28.88	4.33	2.51
2780	3.9	-0.6	29.38	3.92	2.50
2781	3.8	-0.5	29.85	3.61	2.50
2782	3.8	-0.4	30.07	3.46	2.52
2783	4.1	-0.5	29.88	3.60	2.54
2784	4.7	-0.1	29.45	3.92	2.55
2785	5.3	-0.4	29.49	3.63	2.53
2786	5.6	-0.6	29.00	3.93	2.47
2787	5.6	-0.4	29.08	3.67	2.43
2788	5.6	-0.4	28.83	3.70	2.41

Table A9. Floeberg C flight results.

Fiducial No.	AEM Bird			Ice Thick. (m)	Water Depth (m)	Water Conduct. (S/m)
	Pitch (Deg.)	Roll (Deg.)	Elev. (m)			
5740	0.8	-1.3	30.45	2.05	12.86	2.21
5741	1.4	-1.0	31.39	1.19	12.66	2.23
5742	1.6	-0.6	32.41	0.79	12.36	2.20
5743	2.4	-0.3	31.98	1.22	12.36	2.23
5744	3.3	-0.8	30.92	1.61	12.51	2.18
5745	3.4	-0.2	29.68	2.02	12.75	2.19
5746	4.7	-0.9	29.79	1.83	12.71	2.26
5747	5.1	-1.2	30.69	1.47	12.57	2.22
5748	5.0	-1.3	31.43	1.04	12.32	2.18
5749	4.3	-1.3	30.70	1.41	12.31	2.21
5750	3.1	-1.3	29.33	1.95	12.23	2.22
5751	3.6	-1.5	28.76	1.80	12.21	2.26
5752	3.6	-1.4	29.18	1.55	12.03	2.30
5753	4.1	-1.4	30.52	1.14	11.78	2.27
5754	5.0	-0.7	31.23	1.27	11.59	2.26
5755	4.5	-0.6	31.15	1.33	11.60	2.22
5756	4.6	-0.6	29.95	1.85	11.84	2.25
5757	4.7	-0.8	29.64	1.77	11.90	2.26
5758	5.0	-1.2	30.35	1.38	11.81	2.24
5759	5.5	-1.2	31.13	1.35	11.71	2.30
5760	5.6	-1.3	31.51	1.42	11.69	2.23
5761	5.5	-1.3	31.05	1.80	11.71	2.23
5762	5.1	-1.6	30.67	2.01	11.74	2.28
5763	5.1	-1.6	31.23	1.79	11.64	2.32
5764	5.4	-1.4	31.95	1.95	11.31	2.34
5765	5.6	-1.1	33.72	1.04	10.95	2.28
5766	5.6	-0.8	33.77	1.40	10.65	2.35
5767	5.3	-0.6	32.93	1.87	10.32	2.24
5768	5.5	-0.8	32.28	2.00	9.96	2.12
5769	5.8	-0.9	32.85	1.48	9.43	2.05
5770	6.7	-1.2	32.93	1.89	8.92	1.97
5771	6.8	-1.3	33.06	1.89	8.21	1.76
5772	5.7	-1.4	32.10	2.66	7.39	1.47
5773	5.3	-1.5	30.24	3.99	6.82	1.19
5774	5.2	-1.7	30.05	3.99	6.82	0.98
5775	4.9	-1.6	27.79	7.57	5.77	1.01
5776	5.5	-1.1	26.24	10.30	5.56	1.10
5777	5.0	-0.3	26.84	10.30	5.56	0.94
5778	5.1	-0.4	25.99	11.37	5.42	0.94
5779	5.7	-1.0	25.56	12.25	4.44	0.94
5780	6.8	-1.2	26.67	12.25	4.44	0.89
5781	7.7	-1.2	29.20	12.10	4.28	0.78
5782	7.8	-1.7	30.55	12.80	3.97	0.77
5783	7.8	-1.8	29.81	15.09	4.06	0.94
5784	6.3	-1.6	30.19	15.83	3.44	1.07
5785	5.8	-1.9	32.01	14.95	3.83	0.95
5786	6.1	-1.7	34.33	14.95	3.83	0.88
5787	6.3	-1.3	38.60	12.27	3.69	0.88
5788	6.4	-0.8	39.93	12.27	3.69	0.88
5789	5.5	-0.2	40.22	12.40	3.76	0.88
5790	5.1	-0.4	37.72	13.76	3.67	0.76
5791	5.1	-0.6	36.22	14.61	3.81	0.78
5792	5.7	-0.7	36.44	14.69	3.77	0.79
5793	6.2	-1.0	35.90	15.61	4.02	0.89
5794	6.2	-1.3	33.39	17.72	3.60	4.15
5795	5.0	-1.2	29.80	19.33	6.40	4.15

Table A9 (cont'd). Floeberg C flight results.

Fiducial No.	AEM Bird			Ice Thick. (m)	Water Depth (m)	Water Conduct. (S/m)
	Pitch (Deg.)	Roll (Deg.)	Elev. (m)			
5796	4.4	-1.4	31.22	16.10	3.42	1.27
5797	5.0	-1.7	34.64	14.35	4.02	1.20
5798	5.7	-1.1	35.54	14.35	4.02	1.20
5799	5.8	-0.7	36.90	12.81	3.91	1.20
5800	4.9	-0.4	37.47	12.81	3.91	1.20
5801	4.2	-0.4	34.30	13.64	3.73	1.20
5802	4.3	-0.4	33.37	13.80	3.86	1.20
5803	5.3	-0.9	36.02	11.67	3.64	1.20
5804	5.8	-0.9	39.56	9.43	3.10	1.20
5805	5.9	-1.1	39.68	9.43	3.10	1.20
5806	5.5	-1.3	36.82	12.10	3.87	1.00
5807	4.9	-1.6	33.21	15.18	3.93	1.37
5808	5.7	-1.8	34.89	13.92	3.67	1.45
5809	6.0	-1.4	37.15	13.92	3.67	1.30
5810	5.8	-1.0	39.35	12.49	3.61	1.32
5811	4.8	-0.4	38.67	13.28	3.73	1.38
5812	3.9	-0.3	38.96	13.28	3.73	1.38
5813	4.4	-0.5	38.14	12.42	3.87	1.38
5814	5.2	-0.6	40.23	12.42	3.87	1.38
5815	6.6	-1.2	46.46	6.87	4.24	1.38
5816	6.9	-1.6	48.19	5.55	4.23	1.38
5817	5.8	-1.5	45.12	8.88	4.22	1.38
5818	5.0	-1.6	43.04	10.51	4.01	1.38
5819	5.2	-1.7	41.48	12.44	3.60	1.38
5820	5.6	-1.5	43.59	12.44	3.60	1.38
5821	4.9	-0.8	45.99	10.49	3.66	1.38
5822	4.1	-0.1	44.23	10.49	3.66	1.38
5823	3.2	-0.1	42.11	11.22	3.83	1.38
5824	3.7	-0.3	38.02	12.77	3.74	1.38
5825	4.3	-0.8	36.18	13.25	5.25	1.38
5826	5.6	-1.0	38.26	11.03	4.79	1.38
5827	6.5	-1.5	40.36	8.43	4.69	1.38
5828	6.0	-1.4	40.28	7.83	4.96	1.38
5829	5.3	-1.5	37.04	9.97	5.29	1.38
5830	4.8	-1.8	37.94	7.86	6.17	1.38
5831	4.7	-1.6	38.63	6.44	6.30	1.38
5832	4.7	-1.0	40.40	4.74	6.34	1.38
5833	4.6	-0.7	41.07	3.64	6.89	1.38
5834	4.1	-0.1	39.57	3.64	6.89	1.14
5835	3.8	-0.3	37.54	3.70	7.25	1.28
5836	4.3	-0.4	35.49	3.73	7.46	1.40
5837	5.7	-0.8	35.52	2.95	7.77	1.45
5838	6.4	-1.2	35.37	3.10	8.51	1.55
5839	6.4	-1.3	35.11	2.90	8.85	1.60
5840	5.4	-1.3	33.71	3.04	9.09	1.67

A facsimile catalog card in Library of Congress MARC format is reproduced below.

Kovacs, Austin

Airborne electromagnetic sounding of sea ice thickness and sub-ice bathymetry / by Austin Kovacs, Nicholas Valteau and J. Scott Holladay. Hanover, N.H.: U.S. Army Cold Regions Research and Engineering Laboratory; Springfield, Va.: available from National Technical Information Service, 1987.

iv, 48 p., illus.; 28 cm. (CRREL Report 87-23.)

Bibliography: p. 29.

1. Airborne electromagnetic sounding. 2. Ice thickness. 3. Remote sensing. 4. Sea ice. I. I. Valteau, Nicholas. II. Holladay, J. Scott. III. United States Army. Corps of Engineers. IV. Cold Regions Research and Engineering Laboratory. V. Series: CRREL Report 87-23.

END

FILMED

MARCH, 19 88

DTIC